

1           **Geomorphic imprint of high mountain floods: Insight from the 2022**  
2           **hydrological extreme across the Upper Indus terrain in NW Himalayas**

3   Abhishek kashyap<sup>1</sup>, Kristen L. Cook<sup>2</sup>, Mukunda Dev Behera<sup>1\*</sup>

4   <sup>1</sup>Centre for Ocean, River, Atmosphere and Land Sciences (CORAL), Indian Institute of  
5   Technology Kharagpur, Kharagpur- 721302, West Bengal, India

6   <sup>2</sup>IRD, ISTerre, Université Grenoble Alpes, 1381 Rue de la Piscine, 38610 Gières, France

7   **Emails:**

8   Abhishek Kashyap: [kashyap95abhishek@kgpian.iitkgp.ac.in](mailto:kashyap95abhishek@kgpian.iitkgp.ac.in)

9   Kristen L. Cook: [kristen.cook@univ-grenoble-alpes.fr](mailto:kristen.cook@univ-grenoble-alpes.fr)

10   (\*Correspondence): Mukunda Dev Behera: [mdbehera@coral.iitkgp.ac.in](mailto:mdbehera@coral.iitkgp.ac.in)

11

12

13

14

15

16

17

18

19

20           **Geomorphic imprint of high mountain floods: Insight from the 2022**  
21           **hydrological extreme across the Upper Indus terrain in NW Himalayas**

22   **Abstract**

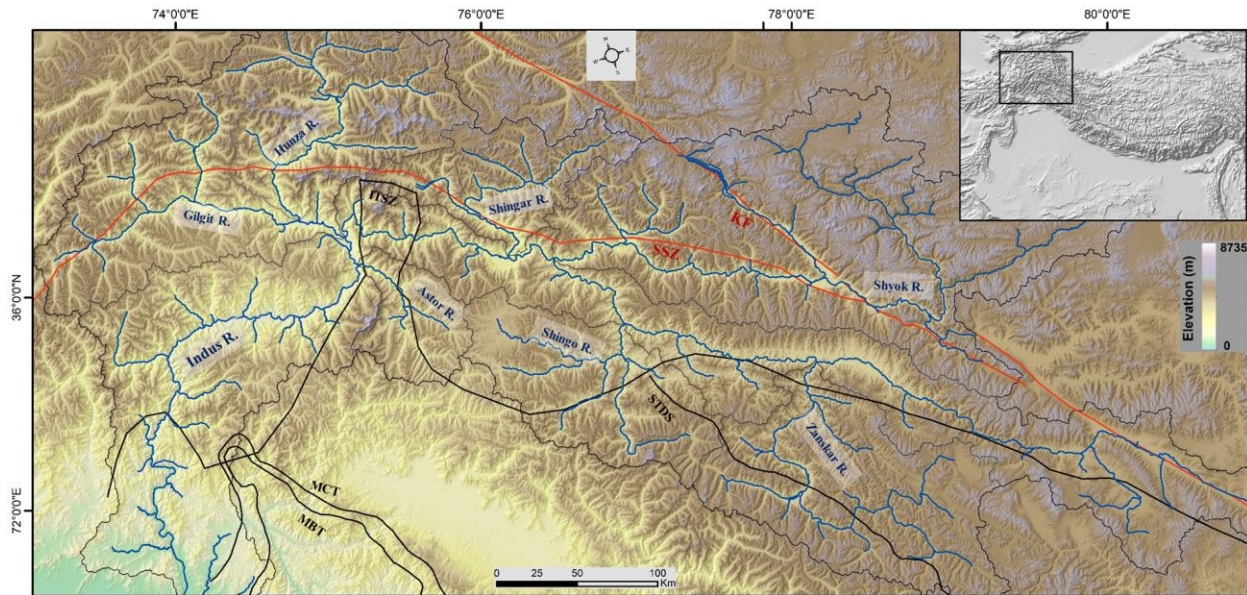
23    The interaction of tectonics, surface processes, and climate extremes impacts how the landscape  
24    responds to extreme hydrological events. An anomalous precipitation event in 2022 occurred  
25    during the monsoon season along the lower middle reaches of the Upper Indus River, resulting in  
26    short-lived high-magnitude flooding and socioeconomic disruption downstream. To understand  
27    the spatial relationship between the geomorphic response and climatic controls of this flood event,  
28    as well as their primary triggers, we performed a landscape analysis using topographic metrics and  
29    quantified the causal association between hydro-climatic variables. Temperature anomalies in  
30    upstream glaciated sub-catchments had a considerable impact on snow cover distribution, based  
31    on our observations. As snow cover changed, glacial melt runoff rose, contributing to increased  
32    fluvial stream power after traversing higher-order reaches. The higher-order reaches of the Upper  
33    Indus River received an anomalously high amount of precipitation, which, when combined with  
34    substantial glacial melt discharge, contributed to an extreme flood across the high-relief steep  
35    gradient channels. The flood-affected regions had a high mean basin  $k_{sn}$  and SL-index, including  
36    numerous spikes in their magnitudes along their channel profiles downstream. To determine how  
37    the lower middle reaches of the Upper Indus River responded to this flood event, we employed the  
38    Enhanced Vegetation Index (EVI) and Normalized Difference Water Index (NDWI) as change  
39    indicator metrics. We observed an inverse causal influence of NDWI on EVI and a statistically  
40    significant relationship between anomalous stream power and relative EVI, suggesting that  
41    downstream channel morphology changed rapidly during this episodic event and highlighting EVI  
42    as a useful indicator of geomorphic change. We suggest that this extreme flood event is a result of  
43    the interaction of anomalous glacial melt and anomalous precipitation over a high-relief landscape,  
44    with a certain causal connection with anomalous temperature over the event duration. The synoptic  
45    observations suggest that this meteorological condition involves the interaction of the Indian  
46    Summer Monsoon (ISM) and Western Disturbance (WD) moisture fluxes. However, the  
47    geomorphic consequences of such anomalous monsoon periods, as well as their influence on long-  
48    term landscape change, are still unclear.

49 **Keywords:** anomalous precipitation; extreme flood; causal relationship; Upper Indus terrain

## 50 **1. Introduction**

51 High mountain floods in the Himalayas are associated with several processes, including coupling  
52 of the Indian Summer Monsoon (ISM) and western disturbance (WD) circulations (Houze et al.,  
53 2011), cloudbursts (Dimri et al., 2016), anomalous precipitation, cloud-scale interconnected  
54 atmospheric anomalies (Dimri et al., 2017), and geomorphic driven surface processes (Sharma et  
55 al., 2017). There is growing recognition that landscapes may evolve through the cumulative effects  
56 of extreme episodic events, in particular in rapidly eroding terrains (Korup, 2012; Cook et al.,  
57 2018). Recent studies suggest that even minor shifts in weather patterns can have a significant  
58 impact on the frequency and magnitude of floods (Knox, 2000; Liu et al., 2015; Benito et al., 2015;  
59 Sharma et al., 2022). It has also been suggested that high-magnitude flood occurrences in the  
60 bedrock rivers draining the Himalayas are the geomorphic agents with the most significant impact  
61 on the evolution of the regional landscape as well as on the residents of the downstream regions  
62 (Bookhagen et al., 2005a; Sharma et al., 2017; Panda et al., 2020).

63 The Tibetan Plateau and its surrounding mountainous regions, such as the Himalayas and  
64 the Karakoram ranges, are critical for the downstream hydrology and water availability of the  
65 Indus River system (Hewitt, 2009; Immerzeel et al. 2010) (Fig.1). The majority of the hydrological  
66 budget of Indus River comes from precipitation, snowmelt, and glaciers, but their relative  
67 contribution varies among the major contributing tributaries (Bookhagen and Burbank 2010; Wu  
68 et al., 2021). The Upper Indus catchment receives precipitation from two distinct climatic systems,  
69 the WD and the ISM, over its foreland and highlands in the northwest (NW) Himalayas  
70 (Bookhagen and Burbank 2006; 2010). However, it remains unclear yet how these two distinct  
71 circulation patterns interact over the Himalayan landscape and what is their potential influence on  
72 long-term geomorphic change (Dimri et al., 2015;2017; Ray et al., 2019).



73

74 Fig.1. Regional topographic setting of Upper Indus catchment along with its major tributaries  
 75 overlaid with major geological structures (MBT= Main boundary Thrust, MCT= Main Central  
 76 Thrust, STDS= Southern Tibet Detachment system, ITSZ= Indus Tibetan Suture Zone, SSZ=  
 77 Shyok Suture Zone, KF= Karakoram fault).

78 Short-duration episodic weather events have a significant influence on hillslope-surface  
 79 processes and rates of bedrock erosion by modulating mass movement and subsequent landscape  
 80 evolution (Snyder et al., 2003; Bookhagen et al., 2005b; Srivastava et al., 2017). During such  
 81 events, a lot of sediment is transported through the fluvial system, some of which is temporarily  
 82 deposited in low-gradient reaches and changes the landscape, before being finally deposited in  
 83 oceanic sinks (Goodbred, 2003; Panda et al., 2020). The geomorphic signatures of catchment  
 84 morphology are vital for understanding and identifying the channel response involved in such  
 85 events as well as the processes and patterns of erosion (Kashyap and Behera., 2023; Sharma et al.,  
 86 2017).

87 From the beginning of July until the end of August 2022, large portions of the Indus catchment  
 88 experienced unprecedented monsoon precipitation (Otto et al., 2023; Nanditha et al., 2023). Some  
 89 recent studies suggest that the primary trigger of this anomalous precipitation event was an  
 90 intensely low atmospheric circulation pattern, low sea surface temperatures across the eastern  
 91 Pacific, and the advent of a La-Nina event (Otto et al., 2023; Nanditha et al., 2023). This extreme

92 precipitation event resulted in a catastrophic flood in the low elevation flood plains of the Indus  
93 catchment (Jones, 2022; Otto et al., 2023; Ma et al., 2023). This severe flood had an extreme  
94 impact over the southern province of Pakistan, causing internal displacement of about ~30–32  
95 million people and the deaths of ~1500–1600 people (Bhutto, 2022; Khokhar, 2022; UNICEF,  
96 2022; Ma et al., 2023). In excess of ~\$25–30 billion in economic losses are anticipated (Bhutto,  
97 2022; Otto et al., 2023). According to reports, the flood in 2022 exceeded the peak flow rate of the  
98 disastrous 2010 floods that occurred over Pakistan (Bhutto, 2022; UNICEF, 2022; Nanditha et al.,  
99 2023). The magnitude of the fluvial discharge over the upstream tributaries of the Indus River  
100 increased predominantly as a result of increased streamflow across glaciated channels (NDMA,  
101 2022; UNICEF, 2022). However, the geomorphic consequences and the main drivers of this high-  
102 magnitude flooding in the Upper Indus catchment have not been evaluated yet.

103 In the present study, we evaluated the spatial distribution of channel changes in the mountainous  
104 portion of the Upper Indus catchment due to the extreme precipitation event in the months of July  
105 and August 2022. We employed a channel slope-discharge product along the trunk channel of the  
106 Upper Indus River to estimate the anomalies in the stream power resulting from the anomalous  
107 precipitation event during July and August 2022. We used a random-forest-based machine learning  
108 approach to compare the observed and predicted intensity of precipitation and runoff by assessing  
109 the mean climatology of independent hydro-climatic variables. We further quantified the causal  
110 relationship between hydro-climatic drivers using nonlinear time series data over the event  
111 duration. We investigated the channel response of this episodic flood event by using the NDWI  
112 and EVI as change indicator metrics and comparing that to event characteristics such as anomalous  
113 precipitation, stream power, and channel metrics. We want to better understand the controls on  
114 where and when these types of extreme hydrological events will substantially modify rivers and  
115 landscapes so associated geomorphic hazards can be better anticipated, and we also want to better  
116 constrain the potential role of these episodic events in driving long-term geomorphic change across  
117 the western syntaxial region.

## 118 **2. Regional Setting**

119 In the Himalayas, the erosion rates are high and the landscape of the mountainous terrain is shaped  
120 by the interactions between river systems and the basement tectonics (Jaiswara et al., 2019; 2020).

121 Among the Himalayan River systems, the Upper Indus is unique, including a fully developed,  
122 ~1200-1400 km long, 8<sup>th</sup>- 9<sup>th</sup>-order drainage that enters the Himalayan terrain as an antecedent  
123 channel and cuts right over the seismically active belt in the Indus- gorges (Fig. 1). This catchment  
124 is highly affected by recurrent landslides or debris flows, and episodic glacial and landslide dams  
125 that represent significant geomorphic hazards (Korup & Montgomery 2008; Korup et al., 2010).

126 The Upper Indus River flows through the highly tectonically active region of the Nanga  
127 Parbat-Haramosh Massif (NP-HM), which is one of the highest relief regions on earth (~>5000  
128 m), and has the strong potential to rapidly erode uplifted material (Leland et al. 1998; Shehzad et  
129 al. 2009; Korup et al. 2010). The NP-HM region experiences the highest recorded rates of  
130 denudation and channel incision on earth (~12 mm/y), as well as high rates of tectonic uplift (~4 -  
131 10 mm/y) and forms river anticlines across extremely weak crust (Koons et al., 2002; 2013; Zeitler  
132 et al., 2001; 2014; Butler, 2019). This has a significant impact on the tectonics and morphology of  
133 the western Himalayas (Hewitt, 2009; Zeitler et al., 2014). The Upper Indus catchment (UIC) is  
134 characterized by extremely steep channel gradient of ~>20-25°, high topographic relief of ~4000–  
135 5000 m, and a large portion of snow-covered peaks (Hewitt, 2007; Farinotti et al., 2020).

136 As a fraction of the total annual discharge, snowmelt constitutes up to 50% in the Upper-  
137 Indus catchment (UIC) (Burbank & Bookhagen, 2006; 2010; Scherler et al., 2011). Due to the  
138 Western Disturbance (WD) inclination, the UIC has a lot of precipitation in the winter and spring  
139 (Kapnick et al., 2014), while due to the orographic barrier of the high mountains, the influence of  
140 the ISM in the region weakens towards to the north-west (Forsythe et al., 2017). The annual  
141 precipitation in the UIC increases with the elevation; across the northern valley floors- in the rain  
142 shadows it ranges from 100-200 mm/y; while at elevation ~4000-4400 ma.s.l., it ranges from 600-  
143 800 mm/y; and above >~5000 ma.s.l., it ranges from 1500 -2000 mm/y (Sharif et al., 2013; Wu et  
144 al., 2021). From October to March, the monthly mean temperatures in the UIC are below freezing  
145 at elevations > ~3000 m (Archer, 2004). Discharge in the tributary channels of the Upper Indus  
146 River that depend on glacier meltwater has a strong association with summer time mean air  
147 temperatures across the Karakoram ranges (Forsythe et al., 2017; Wu et al., 2021).

### 148 **3. Materials and Methodology**

#### 149 **3.1 Data Used**

150 In the present study, we used a 30 m SRTM digital elevation model (DEM) for landscape  
151 characterization and geomorphic quantitative parameter estimation. To investigate the impact of the  
152 climatic variables driving this extreme event on regional erosion processes, we utilized daily  
153 precipitation datasets spanning 40 years (1982–2022) from July 1 to August 31 from CHIRPS  
154 (Climate Hazards Group Infrared Precipitation with Station Data) (Version 2.0 Final). Several  
155 previous studies have investigated CHIRPS precipitation datasets at daily, monthly, and annual  
156 temporal scales across the Indus Basin (Gao et al., 2018; Ullah et al., 2019; Nawaz et al., 2021;  
157 Shahid et al., 2021). In their studies, they extensively evaluated CHIRPS's performance against  
158 regional ground datasets obtained from meteorological stations. Several studies (Katsanos et al.,  
159 2016, Paredes-Trejo et al., 2017, Bai et al., 2018, Gao et al., 2018) suggest CHIRPS for  
160 hydrological analysis and water resource management due to its fine spatiotemporal resolution.

161 We investigated the spatiotemporal distribution of hydrometeorological variables using daily  
162 datasets from July 1 to August 31. The ERA5-Land Daily Aggregated-ECMWF Climate  
163 Reanalysis, which had a spatial resolution of 11132 meters, provided data on 2-meter air  
164 temperature, skin temperature, dewpoint temperature, snowmelt, and runoff. We used remote  
165 sensing-based indices to detect signatures of anomalous changes over the landscape. We computed  
166 these metrics over the monthly mean for July and August 2022, using daily datasets of the MODIS-  
167 based normalized difference water index (NDWI), the normalized difference snow index (NDSI),  
168 snow albedo, EVI, and surface reflectance bands b1 and b2, which have a 500-meter spatial  
169 resolution.

### 170 **3.2 Drainage network extraction and landscape analysis.**

171 We extracted the drainage network from the DEM using the ArcGIS platform. A regional slope  
172 map was produced by running a 1000 m radius mean filter over the slope model derived from the  
173 DEM, and a regional relief map was generated by passing a 1000 m circular radius focal range  
174 window over the DEM. Further analysis of the DEM and the derived flow accumulation data were  
175 performed in MATLAB using the transient profiler tools (Jaiswara et al., 2019, 2020). We  
176 extracted the longitudinal profiles of the bedrock channels within an accumulation region of about  
177  $1 \times 10^6 \text{ m}^2$  and channel network of the Upper Indus catchment using TopoToolbox (Wobus et al.,  
178 2006; Kirby and Whipple, 2012; Schwanghart and Scherler, 2014). We used a 1000 m smoothing

179 window and a 20 m vertical interval to sample the channel networks in order to reduce the noise  
180 and artefacts that are embedded in the elevation data.

### 181 **3.3 Quantitative Geomorphic parameters**

182 We used geomorphic quantitative parameters such as SL (Stream length-gradient index)-index,  $k_{sn}$   
183 (Normalized steepness index) and Stream power of the Upper Indus trunk channel to evaluate the  
184 influence of the high magnitude flooding event across the Upper Indus River during July and  
185 August 2022. To evaluate the spatial variability of the flood magnitude and the channel  
186 morphology, these metrics are plotted on the longitudinal profile of the trunk channel.

#### 187 **3.3.1 Stream length-gradient index (SL- Index)**

188 Rivers often achieve an equilibrium or steady state between erosion and sedimentation, which is  
189 represented by a concave longitudinal river profile (Schumm et al., 2002). Tectonic, lithological,  
190 and/or climatic factors often result in shifts in river profiles from this expected steady-state  
191 condition (Hack, 1973; Burbank and Anderson, 2011). Here, we use the Stream Length-Gradient  
192 (SL) index to identify the zones of topographic break and changes in the channel gradient of the  
193 longitudinal profile by using the equation:

$$194 \quad \quad \quad SL = (\Delta H/\Delta L)/L \dots \dots \dots (1)$$

195 where SL denotes the steepness or gradient of the profile for the local reach, L is the total river  
196 length from the midpoint of the local reach to the highest point on the channel,  $\Delta H$  is the change  
197 in elevation over the reach and  $\Delta L$  is the length of the reach, so  $\Delta H/\Delta L$  represent the channel slope  
198 or gradient of the reach. A sharp lithological variation and/or the differential uplift across active  
199 structures are frequently linked to an abrupt change in SL-index along the river (Hack, 1973;  
200 Jaiswara et al., 2020; Kashyap et al., 2024).

#### 201 **3.3.2 Channel Steepness index**

202 We extracted the bedrock profile of the Upper Indus River, which can be described using the power  
203 law relationship between upstream drainage area (A) and channel gradient (S) as (Jaiswara et al.,  
204 2019, 2020; Kashyap et al., 2024):



205 
$$S = k_s A^{-\theta} \dots \dots \dots (2)$$

206 where  $k_s = (E/K)1/n$  is the channel steepness index,  $\theta = (m/n)$  is the channel concavity index,  $m$   
 207 and  $n$  are positive constants,  $E$  is the erosion rate at a steady state (Wobus et al., 2006; Kirby and  
 208 Whipple, 2012). The relative magnitude of  $k_s$  is often related to the surface uplift rate as well as  
 209 the erosional efficiency across a bedrock catchment (Snyder et al., 2003; Wobus et al., 2006).

210 **3.3.3 Stream Power estimation**

211 The normalized steepness index ( $k_{sn}$ ) has emerged as an important topographic metric with  
 212 significant correlation with erosion rate over a wide range of timescales (Wobus et al., 2006;  
 213 Jaiswara et al., 2019; Kashyap et al., 2024). However, one major drawback of  $k_{sn}$  is that it includes  
 214 an assumption of spatially constant precipitation because upstream drainage area is used as a proxy  
 215 for discharge (Adams et al., 2020; Leonard et al., 2023a).

216 In the present study, we incorporate the precipitation intensity into the stream power  
 217 calculation to analyze the anomalous stream power along the trunk channel during the flood event.  
 218 We estimate the precipitation induced stream power using the slope-discharge method, which  
 219 involves multiplying the accumulated flow distance weighted by precipitation with the hyperbolic  
 220 tangent function of the channel gradient along the flow path (Adams et al., 2020; Leonard et al.,  
 221 2023b). The estimation of stream power ( $K_{sn}Q$ ) as a function of channel discharge can be estimated  
 222 as:

223 
$$K_{sn}Q = (S) \times f(\int p * FD) \dots \dots \dots (3)$$

224 where  $S$  is the channel gradient,  $FD$  is the accumulated flow distance,  $p$  is the accumulated  
 225 precipitation (Leonard et al., 2023a; b). Thus,  $K_{sn}Q$  is a normalized version of the channel  
 226 steepness metric that uses the product of channel gradient ( $S$ ) and upstream discharge ( $Q$ )  
 227 estimated from mean precipitation ( $P$ ) as a fluvial discharge proxy. This enables  $K_{sn}Q$  to account  
 228 for the spatial and temporal variability in precipitation along the upper Indus River during the high  
 229 magnitude flood event. Accumulated precipitation resolves spatial patterns well and scales nearly  
 230 linearly with relevant discharges, particularly for large and long-lasting precipitation events (Rossi  
 231 et al., 2016; Leonard et al., 2023a; b).

232 **3.4 Machine learning based approach to model the anomalous event characteristics**

233 The Random Forest (RF) technique is a supervised machine learning method that has been used  
234 as a tree-based ensemble technique and includes a bagging or boot-strapping algorithm (Breiman,  
235 2001; Wolfensberger et al., 2021). In the present study we use a RF based multivariate regression  
236 approach to estimate the anomalous precipitation and runoff intensity in July and August 2022  
237 using the independent variables obtained from classifying variable importance.

238 
$$H(x) = \sum_{i=1}^T h_i(x) \dots \dots \dots (4)$$

239 Where,  $h_i(x)$  denotes the  $i^{\text{th}}$  regression tree output ( $h_i$ ) on sample  $x$ . Therefore, the prediction of  
240 the RF is the mean of the predicted values of all the decision trees.  $T$  denotes the regression trees  
241 for regression prediction.

242 Based on the mean climatology of the last 40 years, we predict the daily anomalous  
243 precipitation and runoff intensity for the 2022 event and compare them with the observed actual  
244 values. We employed the highest significance variables, as well as precipitation and runoff data  
245 from 1982 to 2021, as a training set. We utilized a time series cross-validation approach in this  
246 study to evaluate the Random Forest model's performance in predicting precipitation and runoff  
247 during the Upper Indus catchment's high-elevation flood event in July and August 2022. Given the  
248 temporal dependency and sequential pattern of hydro-climatic data, using a normal K-fold cross-  
249 validation method could result in data leakage by allowing future data to inform past projections.  
250 To address this issue, we employed time series cross-validation to maintain the data within  
251 chronological order. We trained the model using a sliding window method, gradually moving the  
252 training window forward in time with each iteration. Specifically, we designed the first training  
253 window to contain data from the first 30 years, leaving the last 10 years for testing. In each  
254 successive iteration, we increased the training window by one year and retrained the model on the  
255 expanded training set. We trained these models on meteorological variables obtained from the  
256 classification of the most significant, as well as other physical drivers associated with high-  
257 elevation flood episodes in the region. We evaluated the model's performance based on the  
258 accuracy of precipitation and runoff predictions, using metrics such as mean absolute error (MAE),  
259 mean squared error (MSE), and root mean squared error (RMSE) (SI. Table. 1- 2). We computed  
260 these metrics for each rolling window to gain insight into the model's performance across various

261 time periods, especially in the lead-up to the 2022 flood event. To utilize the independent variables  
262 to estimate these event characteristics, we first classify the hydro-climatic variables based on their  
263 higher importance using the RF classification approach. Then, by using the RF multivariate  
264 regression approach, we select only those independent variables with the highest significance to  
265 estimate anomalous precipitation and runoff intensity during the event duration.

### 266 **3.5 Causal discovery among Hydro-climatic variables**

267 Causal methodologies have been utilized to evaluate whether and how changes in one hydro-  
268 climatological variable during anomalous extreme events influence the magnitude of another  
269 (Runge et al., 2019a; Nowak et al., 2020). To understand how an extreme event is regulated over  
270 high mountainous terrain, a temporal investigation of event characteristics is required. Using this  
271 evaluation, we gain insight into how the conditioning hydro-climatic variables that regulate these  
272 extreme events evolve throughout event duration in a catchment (Runge, 2018; Krich et al., 2020).  
273 Understanding directional dependencies is crucial to distinguish them from connections that  
274 cannot be deduced using any statistical model (Kretschmer et al., 2017; Karmouche et al., 2023).

275 In this study, we use causal stationarity, and the absence of contemporaneous causal effects  
276 for the time series datasets using the PCMCI and MCI approaches (Tibau et al., 2022; Runge,  
277 2023). PCMCI is a causal identification technique that combines the Momentary Conditional  
278 Independence (MCI) approach with the PC algorithm (Runge et al., 2019b; Nowack et al., 2020).  
279 Given a set of multivariate time series, PCMCI estimates the time series graph that depicts the  
280 conditional independencies among the time-lagged factors (Runge et al., 2014; 2019a). In addition  
281 to PCMCI, we use the ParCorr linear independence test based on partial correlations is employed  
282 (Runge et al., 2014; 2023).

283 In order to evaluate the meteorological disturbances associated with the Upper Indus Flood of  
284 2022, we identified the causal lag-connection between hydroclimatic variables, with a specific  
285 focus on exploring the meteorological conditions leading up to and during the flood event. We  
286 focused on identifying the short-term meteorological drivers that triggered the anomalous  
287 precipitation-driven high elevation flood and understanding the distribution of its immediate  
288 impacts within the Upper Indus catchment. We emphasize that this study does not attempt to  
289 explore the causality of long-term climatic changes or assess the full geomorphic consequences of

290 the flood on the landscape. We deliberately limit the scope to comprehend the meteorological  
291 conditions and their direct impact on the flood in the July-August 2022 period. By narrowing our  
292 focus to the short-term hydro-climatic interactions, we aim to offer insights into the key  
293 atmospheric processes and their role in shaping the event's severity rather than its broader or  
294 longer-term geomorphic impacts.

295 In the present study we use the daily datasets of hydro-climatological variables and group them  
296 as; Temperature gradient (Tg), including Air temperature, Surface temperature, and Dewpoint  
297 temperature; Rainfall gradients (Rg), including Precipitation intensity, Runoff and Snowmelt; and  
298 anomalous change indicators (Ac) including EVI, NDWI, and NDSI, July 1 to August 31, 2022,  
299 so includes 62 observational intervals. We evaluate the causal interference between these hydro-  
300 climatic variables using the MCI approach with a maximum 2-day lag period ( $\tau_{\max} = 2$ ) and a limit  
301 for significance set to 0.05 ( $\alpha = 0.05$ ), in order to examine the spatially interdependence  
302 relationships among each of these variables during 2-day event periods.

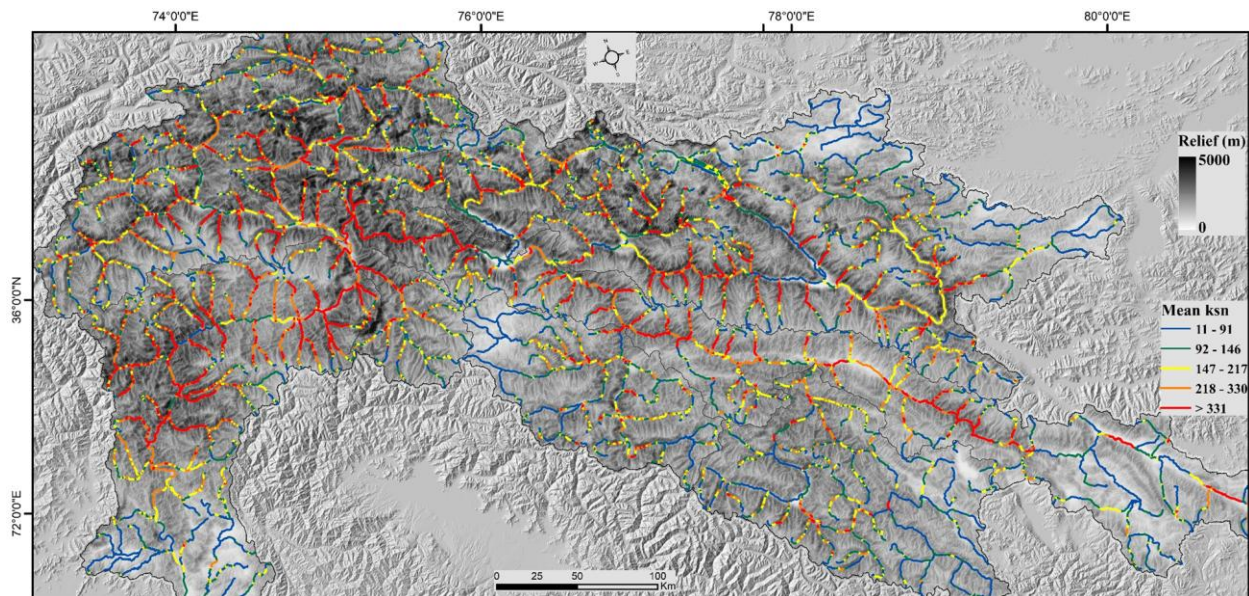
### 303 **3.6 Moisture pathways**

304 The Hybrid Single-Particle Lagrangian Integrated Trajectories (HYSPLIT) model  
305 ([https://www.ready.noaa.gov/HYSPLIT\\_traj.php](https://www.ready.noaa.gov/HYSPLIT_traj.php)) has been employed to determine the probable  
306 moisture parcel source region (Joshi et al., 2023). Over the past decade, researchers have used the  
307 HYSPLIT model to identify moisture sources (Wang et al., 2017; Joshi et al., 2023). To determine  
308 the backward trajectory following an anomalous precipitation event, this study used the HYSPLIT  
309 model. We used three starting heights of 500, 1000, and 3000 ma.s.l. to calculate the backward  
310 trajectory for each day of July and August 2022, given that the HYSPLIT model required the start  
311 date/time, location, and height for each precipitation event (Wang et al., 2017; Gudipati et al.,  
312 2022). This study used meteorological data with a spatial resolution of  $1^{\circ} \times 1^{\circ}$  from the Global Data  
313 Assimilation System (NCEP-GDAS).

## 314 **4. Results**

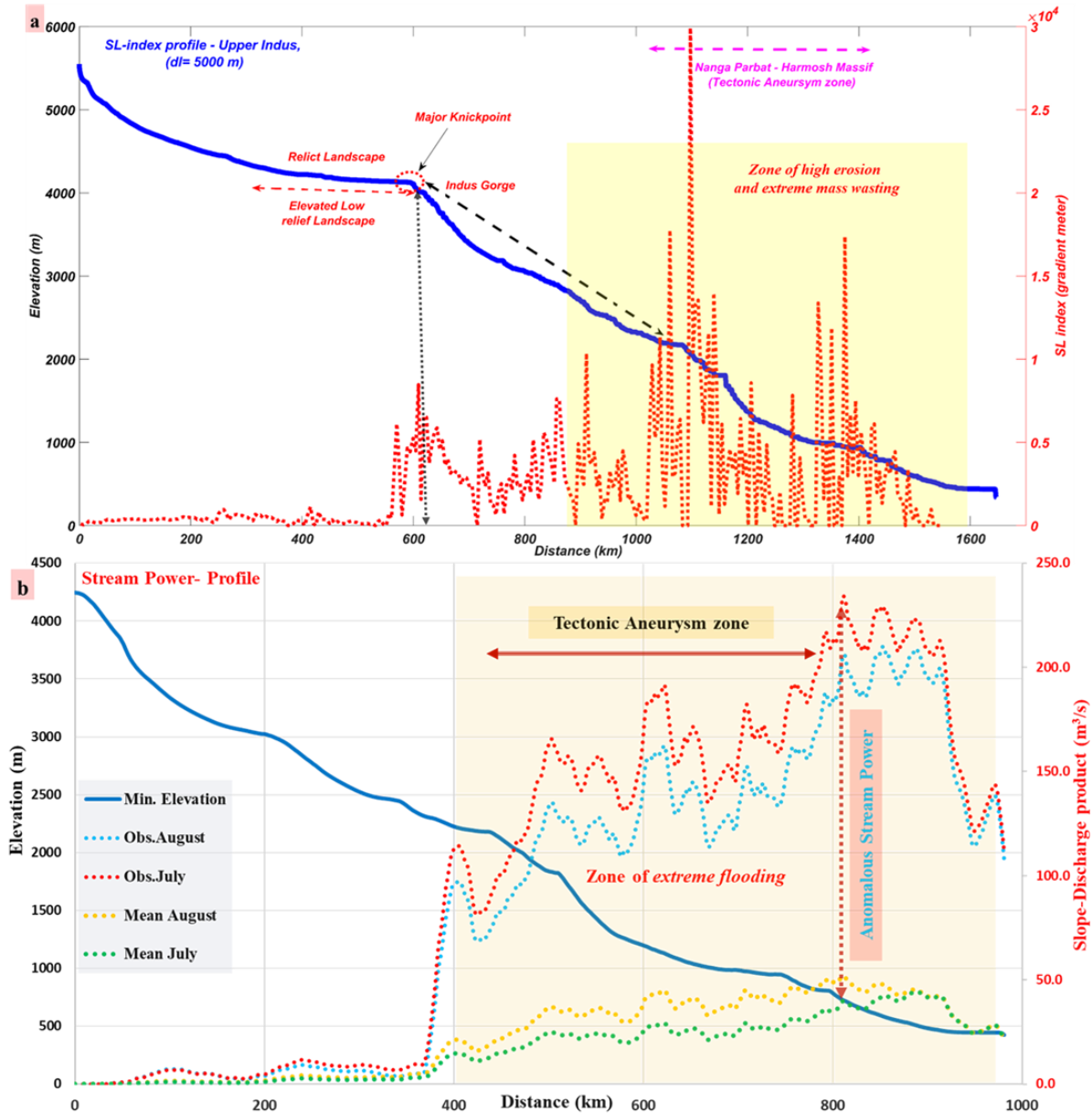
### 315 **4.1 Geomorphic analysis of the Upper Indus terrain**

316 The Indus River is around ~1400–1600 km long and forms multiple loops both parallel to and in  
 317 opposition to the regional structural trend; its bed elevation ranges from ~500-6000–m. The river  
 318 exhibits distinct morphological characteristics over its flow path in terms of its topographic  
 319 attributes and derivatives. Over the elevated low-relief landscape in the Tibetan plateau, the relief  
 320 and channel gradient vary as ( $\sim 0\text{-}500\text{ m}$ ;  $\sim 0\text{-}10^\circ$ ), with a low SL index ( $\sim <1 * 10^4$ ) gradient meter  
 321 and mean basin  $k_{sn}$  of ( $\sim <90\text{ m}^{0.9}$ ) (Fig. 2; Fig. 3a). Then, when the river traverses through the NP-  
 322 HM region, there is a progressive rise in the local relief and channel gradient to ( $\sim >2000\text{-}3000\text{ m}$ ;  
 323  $\sim >25\text{-}35^\circ$ ), which is also reflected in the SL-index ( $>2.5\text{-}3 \times 10^4$ ) and mean  $k_{sn}$  ( $\sim >331\text{ m}^{0.9}$ ). This  
 324 region is characterized by topographic discontinuities across active structures, leading to high  
 325 relief variation and topographic roughness.



326  
 327 Fig.2. Spatial distribution of local relief overlaid with Mean basin  $k_{sn}$  ranges across the Upper  
 328 Indus River catchment.

329 The tributaries in the upstream glaciated valleys that flow parallel to the structural trend  
 330 have a higher mean channel gradient ( $> \sim 20\text{-}30^\circ$ ) and topographic relief ( $> \sim 2000\text{-}3000\text{ m}$ ) (Fig. 2).  
 331 When these tributary channels start to descend towards the main stream after following the  
 332 glaciated landscape, the value of SL and  $k_{sn}$  for the trunk channels shows a significant rise at  
 333  $\sim 3000\text{-}4000\text{ m}$  mean elevation. Approaching the southern mountain front, the main trunk channel  
 334 relief and channel gradient are  $\sim 1000\text{-}2000\text{ m}$  and  $\sim 15\text{-}25^\circ$  respectively (Fig. 3a).



335

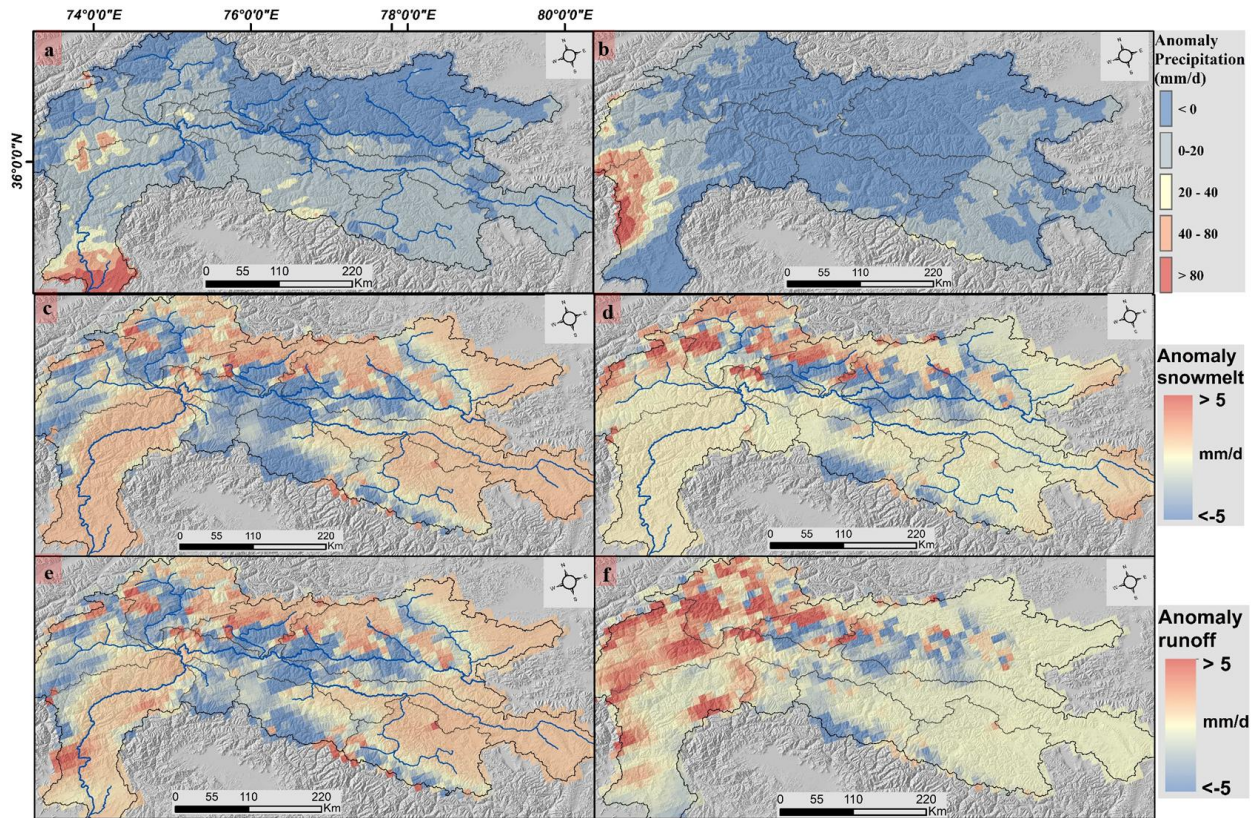
336 Fig.3. The trunk channel profile of Upper Indus River plotted with (a) SL-index; (b) The highest  
 337 order profile of Upper Indus River plotted with Stream power (slope-discharge product)-channel  
 338 elevation (highest order profile is the subset of trunk channel profile indicated by black dash line).

339 The spatial association of higher  $k_{sn}$  ( $>\sim 331 m^{0.9}$ ), topographic relief ( $\sim 1500-2000 m$ ), and  
 340 longitudinal increase in channel gradient along the main Upper Indus River channel downstream  
 341 suggests a higher erosional regime. These high values for the various topographic metrics highlight  
 342 zones of accelerated erosion where the river is in gradational disequilibrium. Furthermore, this

343 tectonically active southern front coincides with a region that gets significant annual mean  
344 precipitation (~1500–2500 mm/y), suggesting a tectonic-climate linkage in the erosional process.

#### 345 **4.2 Spatial distribution of Hydro-climatic anomalies over event duration**

346 The downstream reach of the Upper Indus trunk channel received a significant amount of  
347 anomalous precipitation (>~60–80 mm/d) during the observation period of July and August 2022  
348 (Fig. 4a, 4b). The spatial variability of anomalous precipitation varies with a range of >~0–40  
349 mm/d along its major glaciated tributaries, such as Hunza, Astor, Gilgit, Shingo, and Zaskar. In  
350 July and August 2022, the total extent of anomalous precipitation was around ~900–1000  
351 mm/month, which was approximately ~300–400% more than the long-term (1982–2022) mean  
352 climatology. From July to August 2022, there was continuous precipitation in the high gradient  
353 downstream region, and due to the antecedent weather conditions, extreme precipitation likely  
354 produced suitable conditions for high-magnitude flooding. The potential geomorphic response of  
355 such anomalous precipitation is suggested by the resulting anomalous stream power over the  
356 downstream channels (Fig. 4c, 4d). The spatial distribution of anomalous stream power shows that  
357 the greatest increase occurred at ~400-800 km along the channel profile downstream. For both the  
358 months of July and August of 2022, we observed a significant rise in the stream power, to ~>200  
359 m<sup>3</sup>/s above the mean values (Fig. 3b).

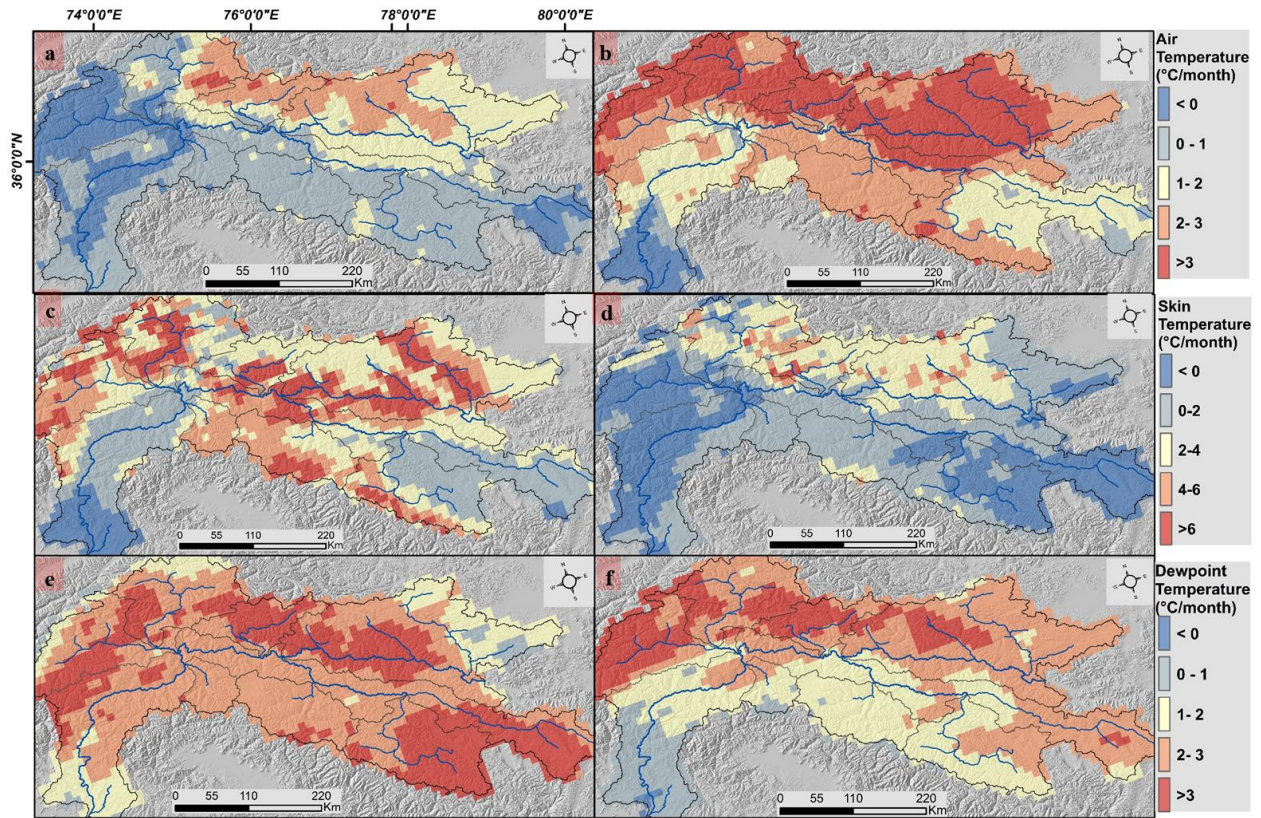


360

361 Fig. 4. Spatial distribution of hydro-meteorological variables for anomalous July and August  
 362 month of 2022 across Upper Indus catchment such as: (a) precipitation (July) (b) precipitation  
 363 (August) (c) Snowmelt (July) (d) snowmelt (August); (e) Runoff (July) (f) Runoff (August).

364 During the observation period, other variables, such as runoff and snowmelt, also showed  
 365 positive anomalies across the upstream glaciated sub-catchments over the Karakoram ranges (Fig.  
 366 4e, 4f). Furthermore, during July and August 2022, the temperature variables indicated a positive  
 367 deviation from the mean climatological trend over the glaciated catchments. In the upstream sub-  
 368 catchments in Shyok, Shingar, Hunza, and Gilgit, air and dewpoint temperatures reach ( $>\sim 3^{\circ}\text{C}$   
 369 above mean), while surface temperatures reach ( $>\sim 6^{\circ}\text{C}$  above mean) (Fig. 5). The spatial  
 370 distribution of anomalous temperatures corresponds well with the anomalous snowmelt and runoff  
 371 magnitude across the upstream glaciated catchments.

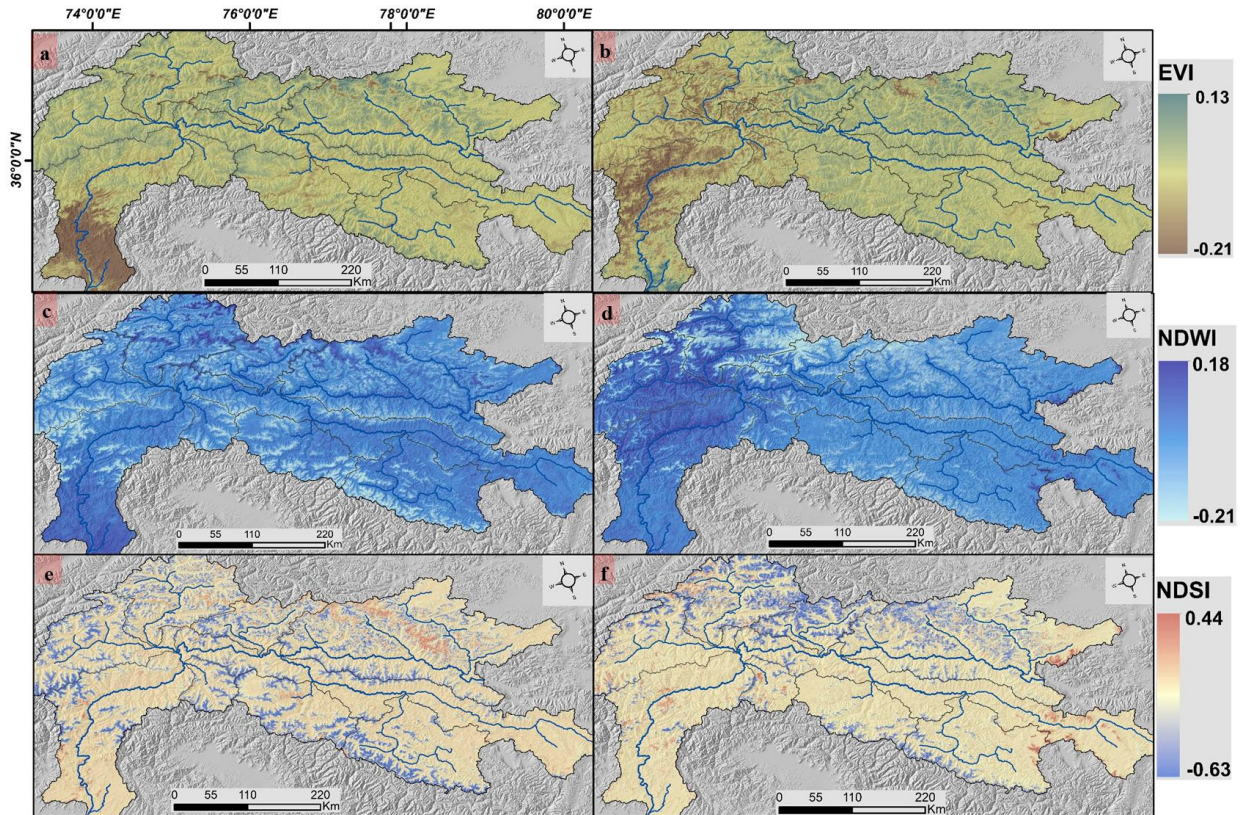




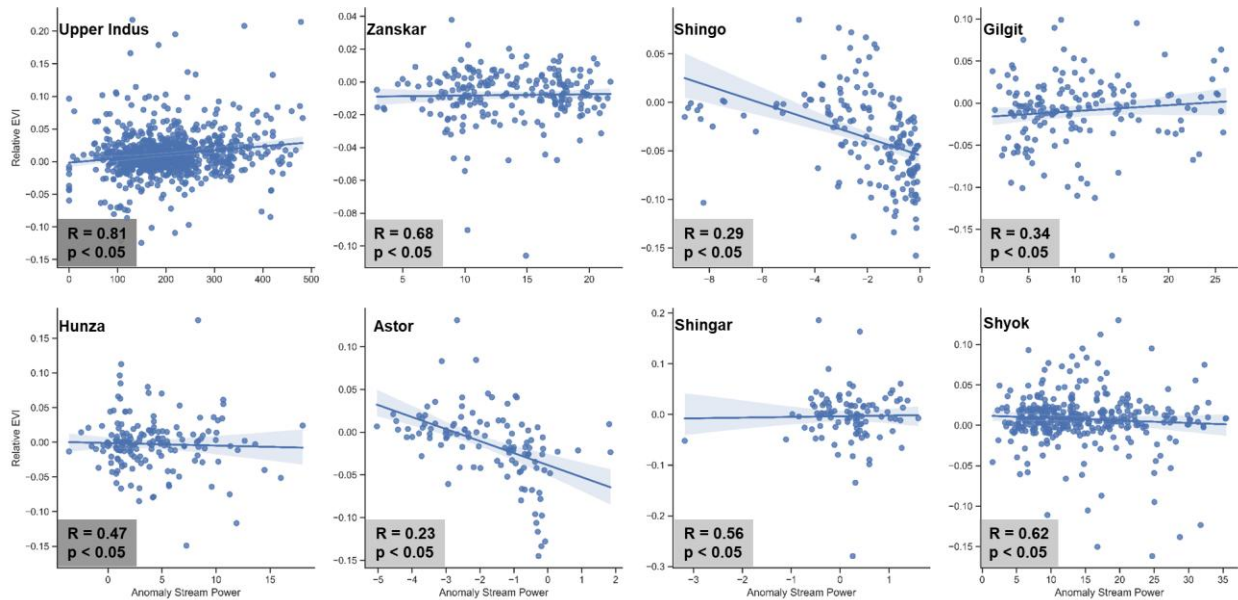
372  
 373 Fig. 5. Spatial distribution of hydro-meteorological variables for anomalous July and August  
 374 month of 2022 across Upper Indus catchment such as: (a) Air temperature (July) (b) Air  
 375 temperature (August) (c) Surface temperature (July) (d) Surface temperature (August); (e)  
 376 Dewpoint temperature (July) (f) Dewpoint temperature (August).

377  
 378 We also observed a significant shift in the spatial distribution of change indicator variables  
 379 during the observation period. In July 2022, the lower middle reaches of the Upper Indus River  
 380 exhibited a negative change in EVI ( $\sim -0.21$ ) and a positive relative NDWI ( $\sim 0.15-0.20$ ). This  
 381 inverse relationship between these two change indicators was found in the upstream channel as  
 382 well in August. During the event, the tributary channels in the upstream glaciated landscape  
 383 experienced a significant change in snow cover distribution, as demonstrated by the spatial  
 384 variations of the relative NDSI ( $\sim 0-0.63$ ). Changes in relative snow cover correspond directly to  
 385 increases in snowmelt and glacial runoff across glaciated catchments (Fig. 6). We observed a  
 386 significant relationship ( $p < 0.005$ ;  $R = 0.81$ ) between the relative EVI metric and the anomalous  
 387 stream power in the Upper Indus trunk channel and along its main tributaries. The anomalous  
 388 stream power of the Upper Indus River and all of its major tributaries corresponds to a proportion

389 of EVI change that exceeds across low-gradient regions. This positive relationship with an  
 390 increasing trend suggests a substantial geomorphic response due to extreme flooding. However, a  
 391 negative relationship between anomalous stream power and EVI can also be observed across the  
 392 channels of Astor and Shingo (Fig. 7).



393  
 394 Fig. 6. Spatial distribution of hydro-meteorological variables for anomalous July and August  
 395 month of 2022 across Upper Indus catchment such as: (a) EVI (July) (b) EVI (August) (c) NDWI  
 396 (July) (d) NDWI (August); (e) NDSI (July) (f) NDSI (August).



398

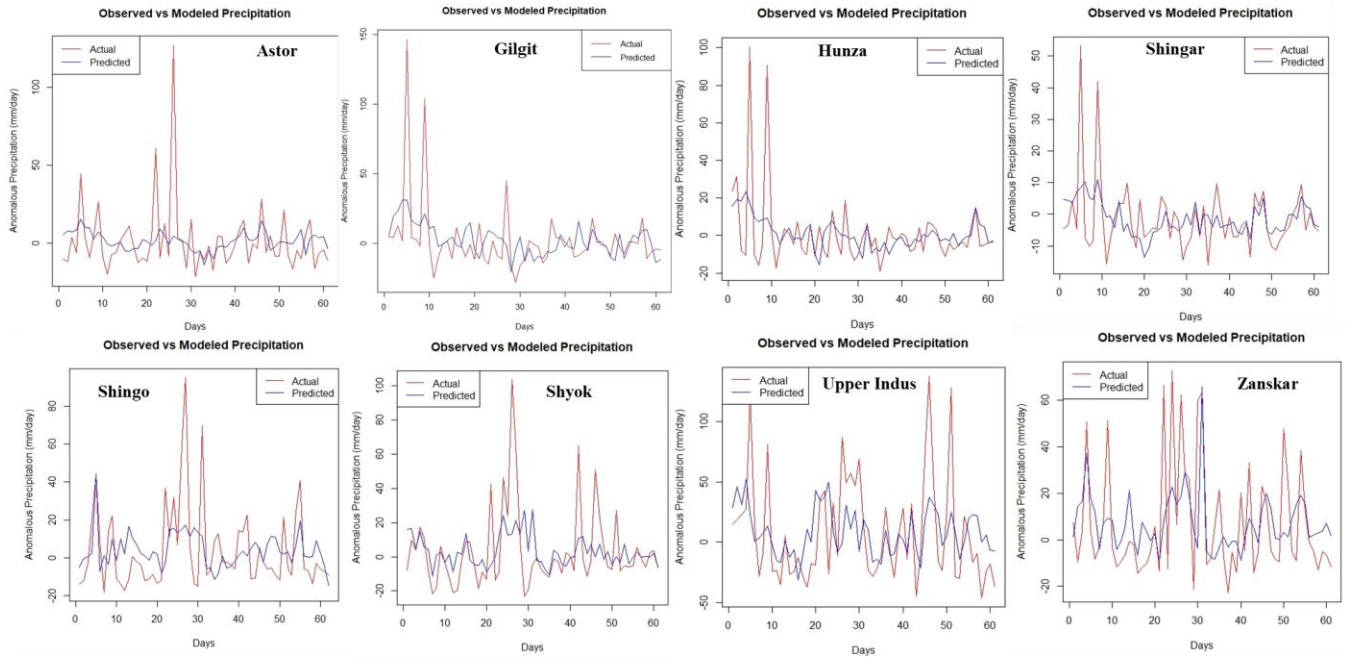
399 Fig.7. Statistical relationship between Relative EVI- Anomalous Stream Power from July 1 to  
 400 August 31, 2022 across Upper Indus catchment as well as along its all the major tributaries.

#### 401 4.3 Machine learning based approach to quantify the event anomalies

402 The RF-classification-based determination of variable importance indicates that dewpoint  
 403 temperature is the most significant variable in estimating precipitation intensity. Other significant  
 404 variables include surface temperature and air temperature. Relative NDSI was the variable of  
 405 highest significance for estimating precipitation in all other sub-catchments except Shingar (Fig.  
 406 S1). Snowmelt, dewpoint temperature, relative NDSI, and surface temperature are the most  
 407 significant variables for each sub-catchment when estimating runoff intensity. Surface temperature  
 408 holds higher significance in the trunk channel catchment of the Upper Indus, followed by air  
 409 temperature and precipitation intensity (Fig. S2). The anomalous precipitation and runoff intensity  
 410 are then estimated using these independent variables with the highest significance obtained during  
 411 classification.

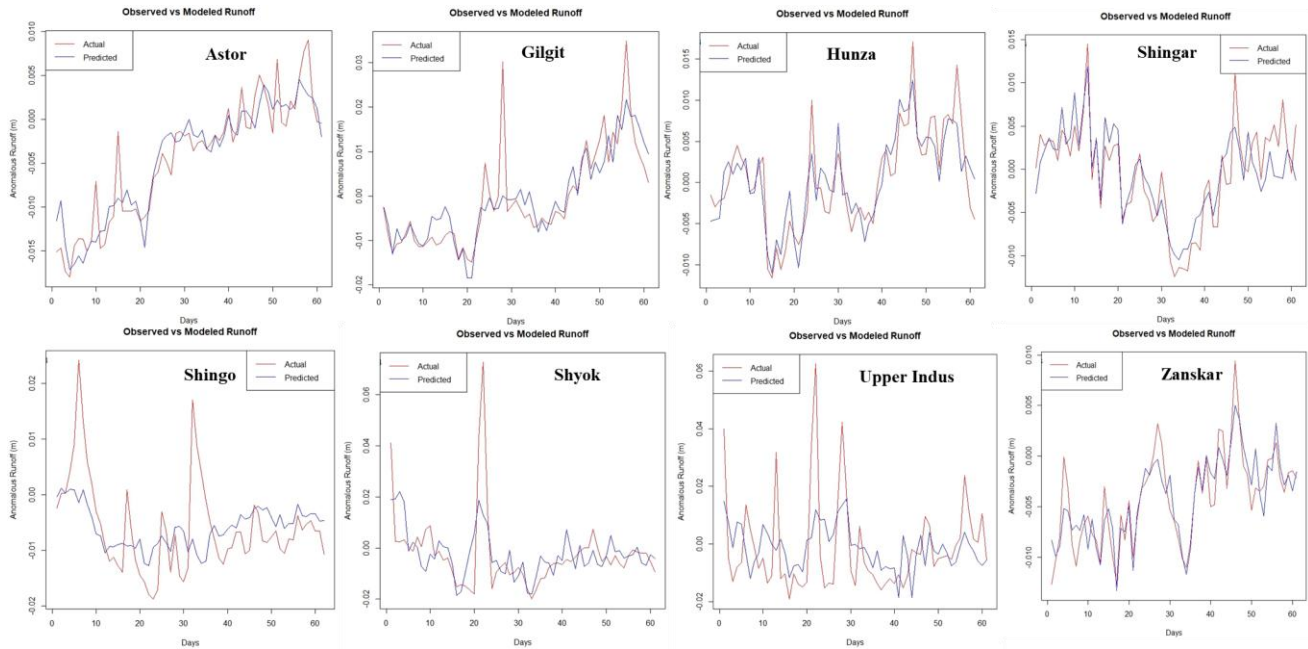
412 The results show that the Upper Indus catchment received significantly more precipitation  
 413 and runoff than predicted at multiple instances in July and August of 2022 (Fig. 8). The anomalous  
 414 and extreme characteristics of the hydro-climatic and terrestrial drivers could explain this  
 415 phenomenon. The Upper Indus catchment received a significant amount of anomalous

416 precipitation, with an intensity of  $>\sim 100$  mm/d, which is much higher than the predicted intensity  
 417 during the period of observation. The channels in the higher relief landscapes such as Astor and  
 418 Gilgit encountered the second-highest anomalous incidence, with intensities  $\sim 80\text{--}100$  mm/d. The  
 419 upstream glaciated catchments, such as the Shyok, Shingo, and Hunza, also have persistent  
 420 anomalous intensities of up to  $\sim 100$  mm/d. The least impacted catchment was Zanskar and Shingo,  
 421 despite a high rate of precipitation that ranges from  $\sim 60\text{--}80$  mm/d.



422  
 423 Fig. 8. Random Forest-Regression based observed vs modeled anomalous precipitation from July  
 424 1 to August 31, 2022 across Upper Indus catchment as well as along all the major tributaries.

425  
 426 The distribution of observed and predicted runoff shows the intensity of observed runoff  
 427 corresponds with the precipitation trend. During the observation period, the Upper Indus  
 428 catchment had much higher runoff rates, followed by upstream glaciated sub-catchments including  
 429 Shyok ( $\sim 30\text{--}60$  mm/d), Shingo, and Gilgit ( $\sim 20\text{--}30$  mm/d). However, in the majority of the  
 430 upstream sub-catchments, the observed anomalous runoff intensity is insignificant (Fig. 9).

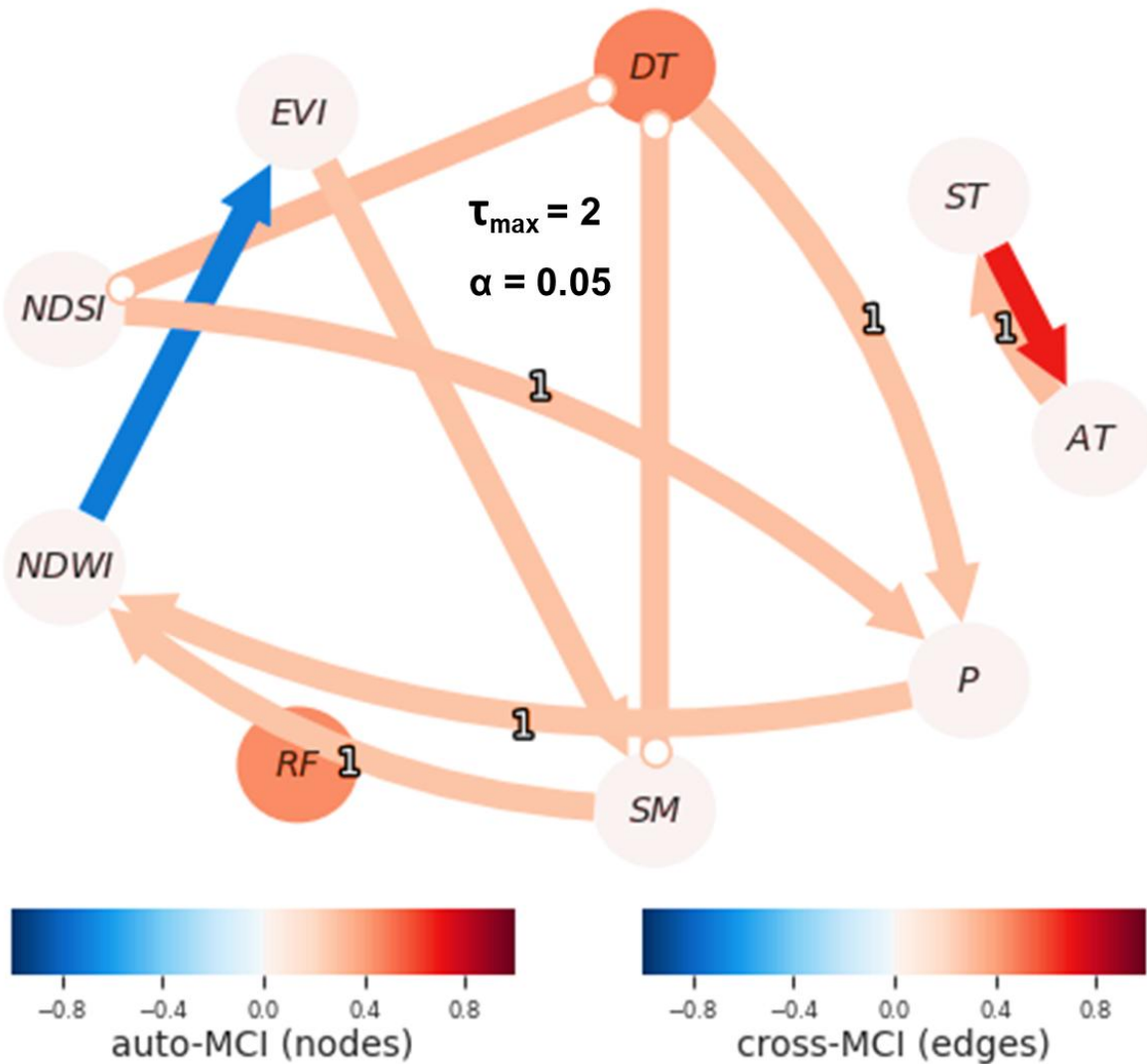


431  
 432 Fig. 9. Random Forest-Regression based observed vs modeled anomalous runoff from July 1 to  
 433 August 31, 2022 across Upper Indus catchment as well as along all the major tributaries.

434 **4.4 Causal relationship among Hydro-climatic variables over event duration**

435 The causal analysis showed that the impact of numerous meteorological variables on the extreme  
 436 flood over the Upper Indus terrain varied significantly. We observed a significant causal lagged  
 437 connection between dewpoint temperature and NDSI, which together positively influenced  
 438 precipitation intensity with a 1-day lag across the Upper Indus catchment. Similarly, precipitation  
 439 intensity and snowmelt exhibit a positive causal influence on NDWI with a 1-day lag period. For  
 440 instance, the cross-correlation between precipitation and dewpoint temperature with positive  
 441 impact is  $> 0.4$  over the event duration. There was a significant negative causal influence of NDWI  
 442 on EVI, indicating an inversely proportional relationship across the observational lag period. The  
 443 hydro-climatic variables such as precipitation intensity, snowmelt, NDWI, EVI, NDSI, air  
 444 temperature, and surface temperature, had non-linear and non-stationary trends from July 1, 2022,  
 445 to August 31, 2022, as shown by the autocorrelation and PCMCi magnitude over the time series.  
 446 The auto MCI ranges of these variables are comparatively very low. Runoff and dewpoint  
 447 temperatures exhibit stationarity and a linear trend over the time series with relative high auto-  
 448 MCI ranges. It is also observed that dewpoint temperature has a significant inherent connection

449 with snowmelt and NDSI, indicating that these variables have a direct causative relationship with  
 450 a high cross-MCI range (Fig. 10). In a causal investigation, edges with arrows indicate a link  
 451 between the drivers. However, depending on the available metrics, there may be an instant causal  
 452 connection between the drivers. It should be observed that this relationship may not have been  
 453 determined to be causative.



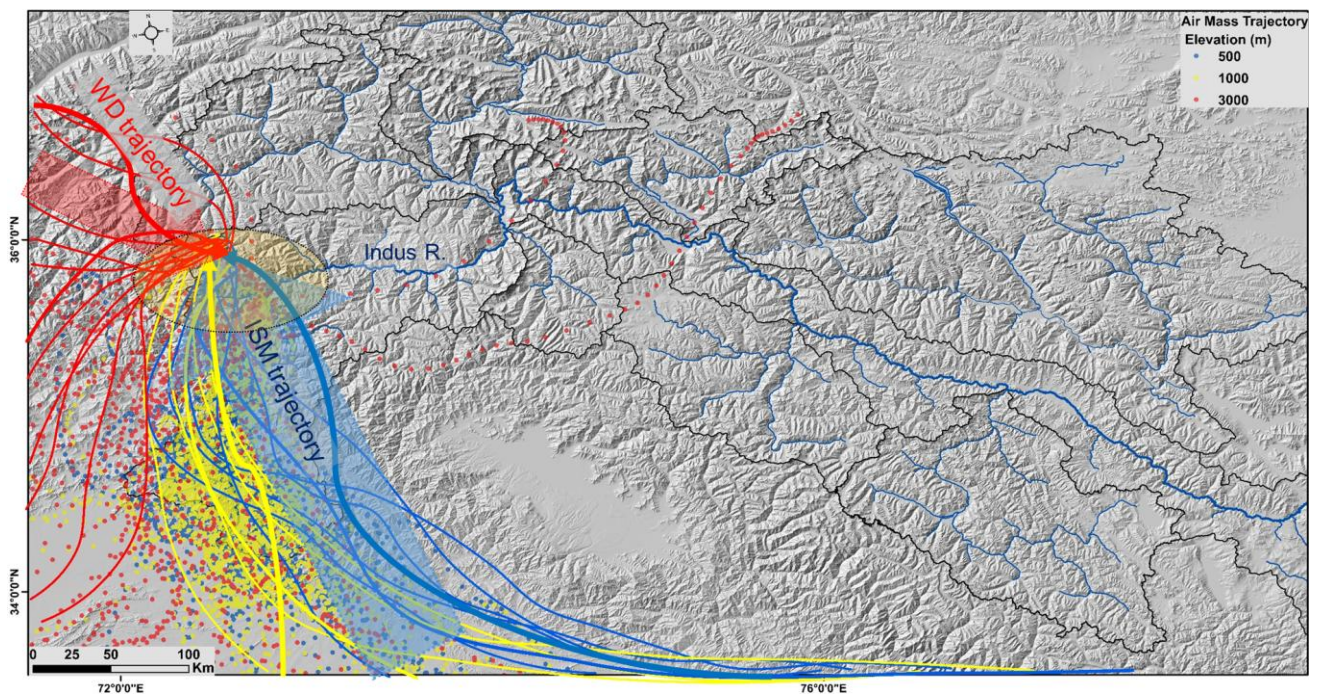
454

455 Fig.10. Causal detection among hydro-climatic driver having non-linear time series from July 1 to  
 456 August 31, 2022 across Upper Indus catchment with maximum allowable lag of 2 days at the 95%  
 457 CI. (The drivers are shown in the solid circles such as: DT= Dewpoint Temperature, ST= Surface  
 458 Temperature, AT= Air Temperature, P= Precipitation intensity, SM= Snowmelt, RF= Runoff,  
 459 NDWI= Normalized Difference Water Index, NDSI= Normalized Difference Snow Index, EVI=

460 Enhanced Vegetation Index: The node color represents autocorrelation whereas link color  
461 represents the strength of directional link. The lag at which the link was found significant is shown  
462 as link label, absence of which indicates that the link was found at zero lag).

#### 463 4.5 Identifying moisture trajectories for the anomalous precipitation event

464 Based on moisture source uptake along trajectories for the observation period of July 1 to August  
465 31, 2022, the amount of precipitation across the orographic ridges of the Upper Indus terrain was  
466 delivered along two major pathways, one from Mediterranean Sea sources such as Western  
467 disturbance (WD)-derived moisture during the onset of the monsoon and a second from the ISM,  
468 originating from the Bay of Bengal and the Arabian Sea. The WD routes provided the moisture  
469 sources for the precipitation along the 3000 m height trajectories, while the Arabian Sea, the Bay  
470 of Bengal, and the Himalayan foreland provided the moisture along the 500 m and 1000 m  
471 trajectories. Furthermore, the anomalous temperature gradient observed for the months of July and  
472 August 2022 shows that the steep bedrock valleys are causing abnormal air-mass feedback. The  
473 substantial divergence in the air-mass curve from mid-July to mid-August 2022 suggests there may  
474 have been very high precipitation and temperature fluctuations during those periods (Fig. 11).



475

476 Fig.11. Moisture pathways (Backward trajectories) for Anomalous precipitation event from July 1  
477 to August 31, 2022 across Upper Indus catchment: (Blue line denotes the trajectory of 500 m  
478 elevation, yellow line denotes the trajectory of 1000 m elevation, and red line denotes the trajectory  
479 of 3000 m elevation: Blue and yellow dot lines exhibit the ISM pathways, whereas Red dot lines  
480 exhibit the WD pathways).

## 481 **5. Discussion**

### 482 **5.1 Spatial relationship between topographic metrics and event anomalies**

483 To characterize the geomorphic response of this extreme flood, we estimated stream power over  
484 the trunk channel of the upper Indus River as an event anomaly. Understanding the spatial  
485 distribution of stream power over the longitudinal profile of bedrock rivers is essential for  
486 evaluating the catchment-scale variability in channel response to anomalous precipitation events  
487 (Whipple et al., 2000; Kaushal et al., 2020). The peaks and troughs in the stream power profile  
488 regulate the morphological characteristics of the bedrock channels (Schneider et al., 2014; Bawa  
489 et al., 2014; Sinha et al., 2017). The river morphology and channel shape will be significantly  
490 impacted by the temporal variations in flooding intensity during anomalous precipitation events  
491 (Bookhagen and Strecker, 2012; Scherler et al., 2014).

492 The initial ~400–600 km length of the Upper Indus River is characterized by low gradient  
493 channels as the river traverses over the elevated-low relief landscape. After traversing through the  
494 mainstream and joining in the highest-order channel across the syntaxial region, there is a sharp  
495 rise in the stream power profile along the downstream. The western syntax (NP-HM) in the NW  
496 Himalayas is one of the most rapidly uplifting ( $>\sim 5\text{-}10$  mm/y) and eroding ( $>\sim 10$  mm/y) regions  
497 on earth, with extreme topographic relief ( $>3000$  m) (Fig. 1; 2). The sudden increase in the stream  
498 power of the Upper Indus River after traversing through NP-HM and the resultant extreme flood  
499 along lower middle reaches were also attributed to this high elevation change ( $>\sim 4000$  m) and  
500 steep channel gradient ( $>\sim 20\text{-}30^\circ$ ) (Fig. 3b). The spatial variability of stream power is also highly  
501 connected with other topographic metrics such as the  $k_{sn}$  and SL index, which demonstrate a  
502 considerable rise in their longitudinal profiles when the channel crosses the NP-HM region (Fig.  
503 3a). We observed that the stream power distribution along the longitudinal profiles of the Upper  
504 Indus River is characterized by numerous peaks for both anomalous precipitation months in July



505 and August 2022 (Fig. 3b). The present study of estimating stream power driven by anomalous  
506 precipitation identifies regions across the Upper Indus catchment with high erosive potential  
507 during the 2022 flood event. However, field validation or high-resolution pre- and post-event  
508 DEMs are required to quantify the rate of erosion and patterns triggered by this extreme flood  
509 event. Our analysis primarily draws upon pre- and post-observations from remote sensing-based  
510 indices, and topographic analysis to spatially correlate estimated stream power with channel  
511 metrics.

512         The upstream glaciated channels of the Trans Himalayan and Karakoram ranges have a  
513 substantial glacial influence on erosion, contributing to the main trunk channel of the Upper Indus  
514 River. Therefore, such high-magnitude floods ought to propagate through the channels of high  
515 mountainous tributaries like Shyok, Gilgit, and Hunza, depending on the landscape characteristics  
516 of the upper Indus catchment. A moderate change in the distribution pattern of snow cover may  
517 have a significant impact on glacial runoff and substantially contribute to fluvial discharge. In  
518 addition to the southern mountain front, the headwaters and syntaxial zone of the Upper Indus  
519 catchment received a significant amount of precipitation, which contributed to the anomalous rise  
520 in stream power and substantially contributed to this extreme flood that influenced the channel  
521 geometry of the lower middle reach and drove high bedrock erosion (Fig. 4). However, the lower  
522 middle reaches with higher stream power are distinguished by the steep channel valley and absence  
523 of sediment deposition. The observation suggests that the higher-order channels of the Upper Indus  
524 River traversing across higher relief and steep gradient valleys likely possess direct first-order  
525 control over the pattern of erosion when combined with an anomalous rate of precipitation (Fig.  
526 3b).

## 527 **5.2 Hydrological extremes and causal connections**

528 Our observations suggest that the interaction of glacial runoff with fluvial discharge over the steep  
529 gradient channels combined to drive the extreme flood event across the Upper Indus catchment.  
530 These extreme hydrological episodes imply that the possible response of atmospheric instabilities  
531 may be elevation-dependent (Dimri et al., 2015; Forsythe et al., 2017; Ullah et al., 2021; Sharma  
532 et al., 2021). It commenced with anomalous rises in temperature gradients over the glaciated sub-  
533 catchments of the Upper Indus terrain, which drove the rapid changes in snow cover distribution

534 (Fig. 5; 6). This directly impacts glacial runoff magnitude and contributes to an anomalous rise in  
535 fluvial stream power when traversed downstream over higher-relief fluvial reaches (Fig. 6). The  
536 lower middle reaches of the Upper Indus catchment witnessed an anomalous amount of  
537 precipitation intensity from early July to late August 2022 (Fig. 4). When compared to the annual  
538 mean climatology, the precipitation intensity in the lower middle reaches of the Upper Indus River  
539 was roughly ~150–200% higher in the 2022 monsoon period. The 2022 Upper Indus flood  
540 represents an abrupt change from the region's prior precipitation and runoff patterns. To study this  
541 anomaly, we utilized a Random Forest model trained on climatological data from the last 40 years  
542 (1982-2021), with an emphasis on the months of July and August. The model used previous  
543 climatology as a training dataset to estimate precipitation and runoff, which are significant drivers  
544 of flooding. Despite the Random Forest model's resilience, the results revealed a substantial  
545 difference between the model's predictions and the actual observed data obtained from the 2022  
546 flood event. The model, based on 40 years of past data, failed to capture the high precipitation and  
547 runoff patterns observed in July and August 2022 (Fig. 8: 9). The model's inability to predict  
548 rainfall intensity, as well as subsequent runoff, highlights the anomalous nature of the event. This  
549 disparity demonstrates that the 2022 flood was not only unusual but also went outside the typical  
550 climatological shifts observed over the previous four decades. This emphasizes the necessity for  
551 future modeling efforts to include other predictors, such as changes in snowmelt dynamics,  
552 atmospheric circulation anomalies, and other non-stationary phenomena.

553 The moisture flux trajectories observed during the 2022 monsoonal period across the lower  
554 middle reaches of the upper Indus River reveal two distinct sources of moisture pathways,  
555 indicating that the combined effect of the westerlies-driven precipitation and the active monsoon  
556 phase has likely caused this episodic event (Wang et al., 2017) (Fig. 11). Over the past years, the  
557 interactions between moisture-laden ISM and southward-penetrating upper-level WD depression  
558 have been linked to some catastrophic western Himalayan floods, such as in 2010 across Pakistan  
559 and 2013 in Uttarakhand, India (Rasmussen and Houze, 2012; Vellore et al., 2015; Dimri et al.,  
560 2016; Sharma et al., 2017). This anomalous rise in the rate of precipitation intensity contributes to  
561 the rapid increase in stream power across steep valleys. The combined causal influence of  
562 temperature and precipitation intensity with topography plays an important role in modulating such  
563 episodic events, as these variables eventually regulate the amount of solid precipitation, influence  
564 the change in snow cover, and have a significant impact on snowmelt runoff (Fig. 10) (Bovy et al.,

565 2016; Godard and Tucker, 2021; Delaney et al., 2023). This flood indicates the importance of  
566 understanding the cause-and-effect relationship between temperature and precipitation in high-  
567 elevation uplands.

### 568 **5.3 Channel Response to an Extreme Flood**

569 This study used the EVI change analysis as a significant event characteristic to capture the  
570 changes in the channel morphology triggered by the 2022 Upper Indus flood. The anomalous  
571 runoff events during the flood significantly altered channel geometry, and these changes were  
572 reflected in the spatial and temporal variations of EVI (Fig. 6). Geomorphic processes such as  
573 inundation, erosion, and landsliding have submerged or removed vegetation in areas marked by  
574 drastic shifts in EVI ranges (Anderson and Goulden, 2011). The reduction in EVI ranges along the  
575 steep channels highlights the expansion of water bodies during flooding, while the surrounding  
576 areas experienced erosion and landslides due to the extreme discharge. The broader geomorphic  
577 consequences of extreme hydrological events, such as river channel widening, sediment  
578 deposition, and riverbank erosion, frequently link to these changes in vegetation cover (Olen et al.,  
579 2016; Starke et al., 2020; Clift and Jonell, 2021; Scheip and Wegmann, 2021). While EVI cannot  
580 directly measure hydrologic parameters, its ability to reflect the loss of vegetation makes it a useful  
581 proxy for assessing the intensity of geomorphic processes during floods. This capability is  
582 particularly important in high-mountain landscapes such as the Upper Indus, where steep  
583 landscapes and glacial fluvial regimes amplify the effects of extreme events.

584 We utilize NDWI and EVI as change indicator metrics to understand the changes in channel  
585 morphology due to this extreme flood event. The spatial variability of EVI corresponds  
586 significantly with an increase in NDWI intensity downstream during July and August 2022 (Fig.  
587 6). The substantial decrease in EVI values along downstream channels has also been attributed to  
588 the anomalous precipitation event, which led to increased surface runoff, higher NDWI limits, and  
589 subsequent flood deposits. We observed a significant direct causal influence with one-day-lagged  
590 connection of precipitation and snowmelt on NDWI (Fig. 10). This combined causal relationship  
591 between precipitation and snowmelt with NDWI intensity indicates that anomalous runoff  
592 occurred across both glacial and fluvial channels. Further the inverse causal connection (negative  
593 MCI ranges) between NDWI and EVI illustrates the rapid change in the channel geometry due to  
594 increase in the fluvial discharge over lower middle reaches (Fig. 10).

595 The change in river morphology driven by the high-magnitude flood episodes is also  
596 documented by the statistically significant ( $p < 0.005$ ;  $R = 0.81$ ) relationship observed between  
597 anomalous stream power and relative EVI across the lower middle reaches of the Upper Indus  
598 River (Fig. 7). It is generally assumed that relative vegetation intensity is an indicator of  
599 geomorphic change that results from short-duration, high-magnitude hydrological events (Olen et  
600 al., 2016; Starke et al., 2020; Clift and Jonell, 2021; Scheip and Wegmann, 2021). Thus, we  
601 anticipate that EVI acts as a spatial indicator of change in the channel morphology across the lower  
602 middle reaches of the trunk channel during the monsoon period of 2022 (Fig. 7) suggesting that  
603 the distribution of event characteristics such as NDWI and EVI can be useful to detect the relative  
604 change in channel morphology triggered by high-magnitude floods.

## 605 **6. Conclusion**

606 Our study reveals several significant event characteristics of the 2022 Upper Indus flood. Our  
607 analysis shows that the Upper Indus flood originated across elevated glacial channels due to the  
608 anomalous temperature rise, which increased the glacial runoff. This increase in runoff across  
609 glaciated catchments after traversing through fluvial reaches enhanced the fluvial discharge and  
610 likely increased the stream power in the anomalous precipitation region. The synoptic observation  
611 of moisture pathways indicates that this anomalous precipitation incident is linked to the  
612 interaction of southward moving mid-latitude westerlies troughs and eastward advancing  
613 southwestern monsoon circulation. We observe a statistically significant relationship between the  
614 anomalous stream power and relative EVI change across the lower middle reaches, which serves  
615 as a significant geomorphic indicator of change in the channel morphology. This will aid in  
616 determining the reliability of EVI as a consistent indicator of geomorphic changes, as well as its  
617 applicability in studying the geomorphic evolution of regional landscapes. This extreme flood  
618 illustrates how causal connections between temperature and precipitation across high relief-  
619 gradient channels can magnify the impacts. Such hydrological events may play significant roles as  
620 efficient geomorphic agents of erosion and, therefore, in the coupling of climatic extremes,  
621 topography, and erosion. This study underscores the susceptibility of the elevated syntaxial region  
622 to short-lived, high-magnitude flooding, indicating the need for additional research to determine  
623 the causal relationship between the drivers of hydrological extremes. Significant research is needed

624 to understand the long-term impact of these extreme climatic events on the geomorphic processes  
625 in the region.

626

627

628

629

630

631

632

633

634

635

636

637

638

639

640

641

642

643

644 **Code and data availability:**

645 The Data used and methodology section includes all of the open-source datasets and tools used in  
646 the study.

647 **Author contribution:**

648 Abhishek Kashyap (AK): Conceptualization, Formal analysis, Methodology, writing – original  
649 draft, Writing – review & editing.

650 Kristen L. Cook (KLC): Supervision, Visualization, Writing – review & editing

651 Mukunda Dev Behera (MDB): Supervision, Validation.

652 **\*Competing interests**

653 The authors declare that they have no known competing financial interests or personal  
654 relationships that could have appeared to influence the work reported in this paper. We wish to  
655 confirm that there are no known conflicts of interest associated with this publication and there has  
656 been no significant financial support for this work that could have influenced its outcome.

657 **Acknowledgments:** The authors acknowledge the authorities of IIT Kharagpur for facilitating the  
658 study. AK thanks the Ministry of Education, Government of India, for the grant of a Ph.D.  
659 Research Fellowship. AK thanks the IRD “South North Scheme” scholarship, managed by  
660 Campus France, for the mobility and facilitation of a major part of this study at ISTerre, Université  
661 Grenoble Alpes.

662

663

664

665

666

667

668 **7. References**

- 669 Adams, B. A., Whipple, K. X., Forte, A. M., Heimsath, A. M., and Hodges, K. V.: Climate  
670 controls on erosion in tectonically active landscapes, *Sci. Adv.*, 6, eaaz3166,  
671 <https://doi.org/10.1126/sciadv.aaz3166>, 2020.
- 672 Anderson, R. G. and Goulden, M. L.: Relationships between climate, vegetation, and energy  
673 exchange across a montane gradient, *J. Geophys. Res.*, 116, G01026,  
674 <https://doi.org/10.1029/2010JG001476>, 2011.
- 675 Archer, D.: Hydrological implications of spatial and altitudinal variation in temperature in the  
676 upper Indus basin, *Hydrology Research*, 35, 209–222, <https://doi.org/10.2166/nh.2004.0015>,  
677 2004.
- 678 Bai, L., Shi, C., Li, L., Yang, Y., and Wu, J.: Accuracy of CHIRPS Satellite-Rainfall Products  
679 over Mainland China, *Remote Sensing*, 10, 362, <https://doi.org/10.3390/rs10030362>, 2018.
- 680 Bawa, N., Jain, V., Shekhar, S., Kumar, N., and Jyani, V.: Controls on morphological variability  
681 and role of stream power distribution pattern, Yamuna River, western India, *Geomorphology*,  
682 227, 60–72, <https://doi.org/10.1016/j.geomorph.2014.05.016>, 2014.
- 683 Benito, G., Macklin, M. G., Panin, A., Rossato, S., Fontana, A., Jones, A. F., Machado, M. J.,  
684 Matlakhova, E., Mozzi, P., and Zielhofer, C.: Recurring flood distribution patterns related to  
685 short-term Holocene climatic variability, *Sci Rep*, 5, 16398, <https://doi.org/10.1038/srep16398>,  
686 2015.
- 687 Bookhagen, B. and Burbank, D. W.: Topography, relief, and TRMM-derived rainfall variations  
688 along the Himalaya, *Geophysical Research Letters*, 33, 2006GL026037,  
689 <https://doi.org/10.1029/2006GL026037>, 2006.
- 690 Bookhagen, B. and Burbank, D. W.: Toward a complete Himalayan hydrological budget:  
691 Spatiotemporal distribution of snowmelt and rainfall and their impact on river discharge, *J.*  
692 *Geophys. Res.*, 115, 2009JF001426, <https://doi.org/10.1029/2009JF001426>, 2010.
- 693 Bookhagen, B. and Strecker, M. R.: Spatiotemporal trends in erosion rates across a pronounced

694 rainfall gradient: Examples from the southern Central Andes, *Earth and Planetary Science*  
695 *Letters*, 327–328, 97–110, <https://doi.org/10.1016/j.epsl.2012.02.005>, 2012.

696 Bookhagen, B., Thiede, R. C., and Strecker, M. R.: Abnormal monsoon years and their control  
697 on erosion and sediment flux in the high, arid northwest Himalaya, *Earth and Planetary Science*  
698 *Letters*, 231, 131–146, <https://doi.org/10.1016/j.epsl.2004.11.014>, 2005a.

699 Bookhagen, B., Thiede, R. C., and Strecker, M. R.: Late Quaternary intensified monsoon phases  
700 control landscape evolution in the northwest Himalaya, *Geol*, 33, 149,  
701 <https://doi.org/10.1130/G20982.1>, 2005b.

702 Bovy, B., Braun, J., and Demoulin, A.: A new numerical framework for simulating the control of  
703 weather and climate on the evolution of soil-mantled hillslopes, *Geomorphology*, 263, 99–112,  
704 <https://doi.org/10.1016/j.geomorph.2016.03.016>, 2016.

705 Burbank, D.W., Anderson, R.S., 2011. *Tectonic geomorphology*. John Wiley & Sons.

706 Butler, R. W. H.: Tectonic evolution of the Himalayan syntaxes: the view from Nanga Parbat,  
707 *SP*, 483, 215–254, <https://doi.org/10.1144/SP483.5>, 2019.

708 Clift, P. D. and Jonell, T. N.: Monsoon controls on sediment generation and transport: Mass  
709 budget and provenance constraints from the Indus River catchment, delta and submarine fan over  
710 tectonic and multimillennial timescales, *Earth-Science Reviews*, 220, 103682,  
711 <https://doi.org/10.1016/j.earscirev.2021.103682>, 2021.

712 Cook, K. L., Andermann, C., Gimbert, F., Adhikari, B. R., and Hovius, N.: Glacial lake outburst  
713 floods as drivers of fluvial erosion in the Himalaya, *Science*, 362, 53–57,  
714 <https://doi.org/10.1126/science.aat4981>, 2018.

715 Delaney, I., Anderson, L., and Herman, F.: Modeling the spatially distributed nature of  
716 subglacial sediment transport and erosion, *Earth Surf. Dynam.*, 11, 663–680,  
717 <https://doi.org/10.5194/esurf-11-663-2023>, 2023.

718 Dimri, A. P., Niyogi, D., Barros, A. P., Ridley, J., Mohanty, U. C., Yasunari, T., and Sikka, D.  
719 R.: Western Disturbances: A review, *Reviews of Geophysics*, 53, 225–246,



720 <https://doi.org/10.1002/2014RG000460>, 2015.

721 Dimri, A. P., Yasunari, T., Kotlia, B. S., Mohanty, U. C., and Sikka, D. R.: Indian winter  
722 monsoon: Present and past, *Earth-Science Reviews*, 163, 297–322,  
723 <https://doi.org/10.1016/j.earscirev.2016.10.008>, 2016.

724 Dimri, A. P., Chevuturi, A., Niyogi, D., Thayyen, R. J., Ray, K., Tripathi, S. N., Pandey, A. K.,  
725 and Mohanty, U. C.: Cloudbursts in Indian Himalayas: A review, *Earth-Science Reviews*, 168,  
726 1–23, <https://doi.org/10.1016/j.earscirev.2017.03.006>, 2017.

727 Fadil, A., 2022. Devastating floods in Pakistan claim lives of more than 500 children. UNICEF.

728 Farinotti, D., Immerzeel, W. W., De Kok, R. J., Quincey, D. J., and Dehecq, A.: Manifestations  
729 and mechanisms of the Karakoram glacier Anomaly, *Nat. Geosci.*, 13, 8–16,  
730 <https://doi.org/10.1038/s41561-019-0513-5>, 2020.

731 Fatima Bhutto: The west is ignoring Pakistan’s super-floods. Heed this warning: tomorrow it will  
732 be you., *The Guardian.*, 9th September, 2022.

733 Forsythe, N., Fowler, H. J., Li, X.-F., Blenkinsop, S., and Pritchard, D.: Karakoram temperature  
734 and glacial melt driven by regional atmospheric circulation variability, *Nature Clim Change*, 7,  
735 664–670, <https://doi.org/10.1038/nclimate3361>, 2017.

736 Gao, F., Zhang, Y., Ren, X., Yao, Y., Hao, Z., and Cai, W.: Evaluation of CHIRPS and its  
737 application for drought monitoring over the Haihe River Basin, China, *Nat Hazards*, 92, 155–  
738 172, <https://doi.org/10.1007/s11069-018-3196-0>, 2018.

739 Godard, V. and Tucker, G. E.: Influence of Climate-Forcing Frequency on Hillslope Response,  
740 *Geophysical Research Letters*, 48, e2021GL094305, <https://doi.org/10.1029/2021GL094305>,  
741 2021.

742 Godard, V., Bourles, D. L., Spinabella, F., Burbank, D. W., Bookhagen, B., Fisher, G. B.,  
743 Moulin, A., and Leanni, L.: Dominance of tectonics over climate in Himalayan denudation,  
744 *Geology*, 42, 243–246, <https://doi.org/10.1130/G35342.1>, 2014.

745 Goodbred, S. L., Kuehl, S. A., Steckler, M. S., and Sarker, M. H.: Controls on facies distribution  
746 and stratigraphic preservation in the Ganges–Brahmaputra delta sequence, *Sedimentary Geology*,  
747 155, 301–316, [https://doi.org/10.1016/S0037-0738\(02\)00184-7](https://doi.org/10.1016/S0037-0738(02)00184-7), 2003.

748 Hack, J.T., 1973. Stream-profile analysis and stream-gradient index. *Journal of Research of the*  
749 *us Geological Survey* 1, 421–429.

750 Hewitt, K.: Tributary glacier surges: an exceptional concentration at Panmah Glacier, Karakoram  
751 Himalaya, *J. Glaciol.*, 53, 181–188, <https://doi.org/10.3189/172756507782202829>, 2007.

752 Hewitt, K.: Catastrophic rock slope failures and late Quaternary developments in the Nanga  
753 Parbat–Haramosh Massif, Upper Indus basin, northern Pakistan, *Quaternary Science Reviews*,  
754 28, 1055–1069, <https://doi.org/10.1016/j.quascirev.2008.12.019>, 2009.

755 Houze, R. A., Rasmussen, K. L., Medina, S., Brodzik, S. R., and Romatschke, U.: Anomalous  
756 Atmospheric Events Leading to the Summer 2010 Floods in Pakistan, *Bulletin of the American*  
757 *Meteorological Society*, 92, 291–298, <https://doi.org/10.1175/2010BAMS3173.1>, 2011.

758 Immerzeel, W. W., Van Beek, L. P. H., and Bierkens, M. F. P.: Climate Change Will Affect the  
759 Asian Water Towers, *Science*, 328, 1382–1385, <https://doi.org/10.1126/science.1183188>, 2010.

760 Jaiswara, N. K., Kotluri, S. K., Pandey, A. K., and Pandey, P.: Transient basin as indicator of  
761 tectonic expressions in bedrock landscape: Approach based on MATLAB geomorphic tool  
762 (Transient-profiler), *Geomorphology*, 346, 106853,  
763 <https://doi.org/10.1016/j.geomorph.2019.106853>, 2019.

764 Jaiswara, N. K., Kotluri, S. K., Pandey, P., and Pandey, A. K.: MATLAB functions for  
765 extracting hypsometry, stream-length gradient index, steepness index, chi gradient of channel  
766 and swath profiles from digital elevation model (DEM) and other spatial data for landscape  
767 characterisation, *Applied Computing and Geosciences*, 7, 100033,  
768 <https://doi.org/10.1016/j.acags.2020.100033>, 2020.

769 Jones, B.: How melting glaciers fueled Pakistan’s fatal floods, , 30th August, 2022.

770 Joshi, S. K., Kumar, S., Sinha, R., Rai, S. P., Khobragade, S., and Rao, M. S.: Identifying

771 moisture transport pathways for north-west India, *Geological Journal*, 58, 4428–4440,  
772 <https://doi.org/10.1002/gj.4759>, 2023.

773 Kamaljit Ray, P. Pandey, C. Pandey, A. P. Dimri, K. Kishore: On the recent floods in India,  
774 *Current Science*, Vol. 117, No. 2, 2019.

775 Kapnick, S. B., Delworth, T. L., Ashfaq, M., Malyshev, S., and Milly, P. C. D.: Snowfall less  
776 sensitive to warming in Karakoram than in Himalayas due to a unique seasonal cycle, *Nature*  
777 *Geosci*, 7, 834–840, <https://doi.org/10.1038/ngeo2269>, 2014.

778 Karmouche, S., Galytska, E., Runge, J., Meehl, G. A., Phillips, A. S., Weigel, K., and Eyring, V.:  
779 Regime-oriented causal model evaluation of Atlantic–Pacific teleconnections in CMIP6, *Earth*  
780 *Syst. Dynam.*, 14, 309–344, <https://doi.org/10.5194/esd-14-309-2023>, 2023.

781 Kashyap, A. and Behera, M. D.: The influence of landslide morphology on erosion rate  
782 variability across western Himalayan catchments: Role of westerlies and summer monsoon  
783 interaction in the landscape characterization, *Geological Journal*, 59, 1112–1125,  
784 <https://doi.org/10.1002/gj.4913>, 2024.

785 Kashyap, A., Behera, M. D., and Pradhan, B.: Differential surface uplift and knickpoint  
786 evolution along the transient Teesta river in the eastern Himalayas, *Journal of Asian Earth*  
787 *Sciences*, 260, 105974, <https://doi.org/10.1016/j.jseaes.2023.105974>, 2024.

788 Katsanos, D., Retalis, A., and Michaelides, S.: Validation of a high-resolution precipitation  
789 database (CHIRPS) over Cyprus for a 30-year period, *Atmospheric Research*, 169, 459–464,  
790 <https://doi.org/10.1016/j.atmosres.2015.05.015>, 2016.

791 Kaushal, R. K., Sarkar, A., Mishra, K., Sinha, R., Nepal, S., and Jain, V.: Spatio-temporal  
792 variability in stream power distribution in the Upper Kosi River basin, Central Himalaya:  
793 Controls and geomorphic implications, *Geomorphology*, 350, 106888,  
794 <https://doi.org/10.1016/j.geomorph.2019.106888>, 2020.

795 Khokhar, M.N., 2022. Rich countries caused Pakistan’s catastrophic flooding. Their response?  
796 Inertia and apathy. *The Guardian*.

797 Kirby, E. and Whipple, K. X.: Expression of active tectonics in erosional landscapes, *Journal of*  
798 *Structural Geology*, 44, 54–75, <https://doi.org/10.1016/j.jsg.2012.07.009>, 2012.

799 Knox, J. C.: Sensitivity of modern and Holocene floods to climate change, *Quaternary Science*  
800 *Reviews*, 19, 439–457, [https://doi.org/10.1016/S0277-3791\(99\)00074-8](https://doi.org/10.1016/S0277-3791(99)00074-8), 2000.

801 Koons, P., Zeitler, P., Chamberlain, C., Craw, D., Meltzer, A., 2002. Mechanical links between  
802 erosion and metamorphism in Nanga Parbat, Pakistan Himalaya. *American Journal of Science*  
803 302, 749–773.

804 Koons, P.O., Zeitler, P., Hallet, B., 2013. Tectonic aneurysms and mountain building. *Treatise*  
805 *on geomorphology* 5, 318–349.

806 Korup, O.: Earth’s portfolio of extreme sediment transport events, *Earth-Science Reviews*, 112,  
807 115–125, <https://doi.org/10.1016/j.earscirev.2012.02.006>, 2012.

808 Korup, O. and Montgomery, D. R.: Tibetan plateau river incision inhibited by glacial  
809 stabilization of the Tsangpo gorge, *Nature*, 455, 786–789, <https://doi.org/10.1038/nature07322>,  
810 2008.

811 Korup, O., Montgomery, D. R., and Hewitt, K.: Glacier and landslide feedbacks to topographic  
812 relief in the Himalayan syntaxes, *Proc. Natl. Acad. Sci. U.S.A.*, 107, 5317–5322,  
813 <https://doi.org/10.1073/pnas.0907531107>, 2010a.

814 Korup, O., Densmore, A. L., and Schlunegger, F.: The role of landslides in mountain range  
815 evolution, *Geomorphology*, 120, 77–90, <https://doi.org/10.1016/j.geomorph.2009.09.017>, 2010b.

816 Kretschmer, M., Runge, J., and Coumou, D.: Early prediction of extreme stratospheric polar  
817 vortex states based on causal precursors, *Geophysical Research Letters*, 44, 8592–8600,  
818 <https://doi.org/10.1002/2017GL074696>, 2017.

819 Krich, C., Runge, J., Miralles, D. G., Migliavacca, M., Perez-Priego, O., El-Madany, T., Carrara,  
820 A., and Mahecha, M. D.: Estimating causal networks in biosphere–atmosphere interaction with  
821 the PCMCi approach, *Biogeosciences*, 17, 1033–1061, <https://doi.org/10.5194/bg-17-1033-2020>,  
822 2020.

823 Lague, D.: The stream power river incision model: evidence, theory and beyond, *Earth Surf*  
824 *Processes Landf*, 39, 38–61, <https://doi.org/10.1002/esp.3462>, 2014.

825 Leland, J., Reid, M. R., Burbank, D. W., Finkel, R., and Caffee, M.: Incision and differential  
826 bedrock uplift along the Indus River near Nanga Parbat, Pakistan Himalaya, from <sup>10</sup>Be and <sup>26</sup>Al  
827 exposure age dating of bedrock straths, *Earth and Planetary Science Letters*, 154, 93–107,  
828 [https://doi.org/10.1016/S0012-821X\(97\)00171-4](https://doi.org/10.1016/S0012-821X(97)00171-4), 1998.

829 Leonard, J. S., Whipple, K. X., and Heimsath, A. M.: Isolating climatic, tectonic, and lithologic  
830 controls on mountain landscape evolution, *Sci. Adv.*, 9, eadd8915,  
831 <https://doi.org/10.1126/sciadv.add8915>, 2023.

832 Leonard, J. S., Whipple, K. X., and Heimsath, A. M.: Controls on topography and erosion of the  
833 north-central Andes, *Geology*, 52, 153–158, <https://doi.org/10.1130/G51618.1>, 2024.

834 Liu, P., Li, L., Guo, S., Xiong, L., Zhang, W., Zhang, J., and Xu, C.-Y.: Optimal design of  
835 seasonal flood limited water levels and its application for the Three Gorges Reservoir, *Journal of*  
836 *Hydrology*, 527, 1045–1053, <https://doi.org/10.1016/j.jhydrol.2015.05.055>, 2015.

837 Ma, Y., Hu, X., Chen, Y., Hu, Z., Feng, T., and Feng, G.: Different Characteristics and Drivers  
838 of the Extraordinary Pakistan Rainfall in July and August 2022, *Remote Sensing*, 15, 2311,  
839 <https://doi.org/10.3390/rs15092311>, 2023.

840 Montgomery, D. R., Balco, G., and Willett, S. D.: Climate, tectonics, and the morphology of the  
841 Andes, *Geol*, 29, 579, [https://doi.org/10.1130/0091-7613\(2001\)029<0579:CTATMO>2.0.CO;2](https://doi.org/10.1130/0091-7613(2001)029<0579:CTATMO>2.0.CO;2),  
842 2001.

843 Nanditha, J. S., Kushwaha, A. P., Singh, R., Malik, I., Solanki, H., Chuphal, D. S., Dangar, S.,  
844 Mahto, S. S., Vegad, U., and Mishra, V.: The Pakistan Flood of August 2022: Causes and  
845 Implications, *Earth's Future*, 11, e2022EF003230, <https://doi.org/10.1029/2022EF003230>, 2023.

846 Nawaz, M., Iqbal, M. F., and Mahmood, I.: Validation of CHIRPS satellite-based precipitation  
847 dataset over Pakistan, *Atmospheric Research*, 248, 105289,  
848 <https://doi.org/10.1016/j.atmosres.2020.105289>, 2021.

849 NDMA, 2022. NDMA monsoon 2022 daily situation report No 093.

850 Nowack, P., Runge, J., Eyring, V., and Haigh, J. D.: Causal networks for climate model  
851 evaluation and constrained projections, *Nat Commun*, 11, 1415, [https://doi.org/10.1038/s41467-](https://doi.org/10.1038/s41467-020-15195-y)  
852 [020-15195-y](https://doi.org/10.1038/s41467-020-15195-y), 2020.

853 Olen, S. M., Bookhagen, B., and Strecker, M. R.: Role of climate and vegetation density in  
854 modulating denudation rates in the Himalaya, *Earth and Planetary Science Letters*, 445, 57–67,  
855 <https://doi.org/10.1016/j.epsl.2016.03.047>, 2016.

856 Otto, F. E. L., Zachariah, M., Saeed, F., Siddiqi, A., Kamil, S., Mushtaq, H., Arulalan, T.,  
857 AchutaRao, K., Chaithra, S. T., Barnes, C., Philip, S., Kew, S., Vautard, R., Koren, G., Pinto, I.,  
858 Wolski, P., Vahlberg, M., Singh, R., Arrighi, J., Van Aalst, M., Thalheimer, L., Raju, E., Li, S.,  
859 Yang, W., Harrington, L. J., and Clarke, B.: Climate change increased extreme monsoon rainfall,  
860 flooding highly vulnerable communities in Pakistan, *Environ. Res.: Climate*, 2, 025001,  
861 <https://doi.org/10.1088/2752-5295/acbfd5>, 2023.

862 Panda, S., Kumar, A., Das, S., Devrani, R., Rai, S., Prakash, K., and Srivastava, P.: Chronology  
863 and sediment provenance of extreme floods of Siang River (Tsangpo-Brahmaputra River valley),  
864 northeast Himalaya, *Earth Surf Processes Landf*, 45, 2495–2511,  
865 <https://doi.org/10.1002/esp.4893>, 2020.

866 Paredes-Trejo, F. J., Barbosa, H. A., and Lakshmi Kumar, T. V.: Validating CHIRPS-based  
867 satellite precipitation estimates in Northeast Brazil, *Journal of Arid Environments*, 139, 26–40,  
868 <https://doi.org/10.1016/j.jaridenv.2016.12.009>, 2017.

869 Piatrunia, N. and 0000-0002-5341-7964: Glacial to Holocene climate variability in the southern  
870 mid latitudes, <https://doi.org/10.26153/TSW/45137>, 2022.

871 Rasmussen, K. L. and Houze, R. A.: A Flash-Flooding Storm at the Steep Edge of High Terrain:  
872 Disaster in the Himalayas, *Bulletin of the American Meteorological Society*, 93, 1713–1724,  
873 <https://doi.org/10.1175/BAMS-D-11-00236.1>, 2012.

874 Rossi, M. W., Whipple, K. X., and Vivoni, E. R.: Precipitation and evapotranspiration controls  
875 on daily runoff variability in the contiguous United States and Puerto Rico, *JGR Earth Surface*,

876 121, 128–145, <https://doi.org/10.1002/2015JF003446>, 2016.

877 Runge, J.: Causal network reconstruction from time series: From theoretical assumptions to  
878 practical estimation, *Chaos: An Interdisciplinary Journal of Nonlinear Science*, 28, 075310,  
879 <https://doi.org/10.1063/1.5025050>, 2018.

880 Runge, J., Gao, P., Garcin, F., and Faltings, B.: Churn prediction for high-value players in casual  
881 social games, in: 2014 IEEE Conference on Computational Intelligence and Games, 2014 IEEE  
882 Conference on Computational Intelligence and Games (CIG), Dortmund, Germany, 1–8,  
883 <https://doi.org/10.1109/CIG.2014.6932875>, 2014.

884 Runge, J., Nowack, P., Kretschmer, M., Flaxman, S., and Sejdinovic, D.: Detecting and  
885 quantifying causal associations in large nonlinear time series datasets, *Sci. Adv.*, 5, eaau4996,  
886 <https://doi.org/10.1126/sciadv.aau4996>, 2019a.

887 Runge, J., Bathiany, S., Bollt, E., Camps-Valls, G., Coumou, D., Deyle, E., Glymour, C.,  
888 Kretschmer, M., Mahecha, M. D., Muñoz-Marí, J., Van Nes, E. H., Peters, J., Quax, R.,  
889 Reichstein, M., Scheffer, M., Schölkopf, B., Spirtes, P., Sugihara, G., Sun, J., Zhang, K., and  
890 Zscheischler, J.: Inferring causation from time series in Earth system sciences, *Nat Commun*, 10,  
891 2553, <https://doi.org/10.1038/s41467-019-10105-3>, 2019b.

892 Runge, J., Gerhardus, A., Varando, G., Eyring, V., and Camps-Valls, G.: Causal inference for  
893 time series, *Nat Rev Earth Environ*, 4, 487–505, <https://doi.org/10.1038/s43017-023-00431-y>,  
894 2023.

895 Scheip, C. M. and Wegmann, K. W.: HazMapper: a global open-source natural hazard mapping  
896 application in Google Earth Engine, *Nat. Hazards Earth Syst. Sci.*, 21, 1495–1511,  
897 <https://doi.org/10.5194/nhess-21-1495-2021>, 2021.

898 Scherler, D., Bookhagen, B., and Strecker, M. R.: Spatially variable response of Himalayan  
899 glaciers to climate change affected by debris cover, *Nature Geosci*, 4, 156–159,  
900 <https://doi.org/10.1038/ngeo1068>, 2011.

901 Schneider, J. M., Turowski, J. M., Rickenmann, D., Hegglin, R., Arrigo, S., Mao, L., and  
902 Kirchner, J. W.: Scaling relationships between bed load volumes, transport distances, and stream

903 power in steep mountain channels: Tracer Erlenbach, J. *Geophys. Res. Earth Surf.*, 119, 533–  
904 549, <https://doi.org/10.1002/2013JF002874>, 2014.

905 Schwanghart, W. and Scherler, D.: Short Communication: TopoToolbox 2 – MATLAB-based  
906 software for topographic analysis and modeling in Earth surface sciences, *Earth Surf. Dynam.*, 2,  
907 1–7, <https://doi.org/10.5194/esurf-2-1-2014>, 2014.

908 Shahid, M., Rahman, K. U., Haider, S., Gabriel, H. F., Khan, A. J., Pham, Q. B., Mohammadi,  
909 B., Linh, N. T. T., and Anh, D. T.: Assessing the potential and hydrological usefulness of the  
910 CHIRPS precipitation dataset over a complex topography in Pakistan, *Hydrological Sciences*  
911 *Journal*, 66, 1664–1684, <https://doi.org/10.1080/02626667.2021.1957476>, 2021.

912 Shahzad, F., Mahmood, S. A., and Gloaguen, R.: Drainage network and lineament analysis: An  
913 approach for Potwar Plateau (Northern Pakistan), *J. Mt. Sci.*, 6, 14–24,  
914 <https://doi.org/10.1007/s11629-009-0206-4>, 2009.

915 Sharif, M., Archer, D. R., Fowler, H. J., and Forsythe, N.: Trends in timing and magnitude of  
916 flow in the Upper Indus Basin, *Hydrol. Earth Syst. Sci.*, 17, 1503–1516,  
917 <https://doi.org/10.5194/hess-17-1503-2013>, 2013.

918 Sharma, S., Shukla, A. D., Bartarya, S. K., Marh, B. S., and Juyal, N.: The Holocene floods and  
919 their affinity to climatic variability in the western Himalaya, India, *Geomorphology*, 290, 317–  
920 334, <https://doi.org/10.1016/j.geomorph.2017.04.030>, 2017.

921 Sharma, S., Sati, S. P., Basavaiah, N., Pandey, S., Sundriyal, Y. P., Rana, N., Singh, P., Pradhan,  
922 S., Shukla, A. D., Bhushan, R., Bhatt, R., and Juyal, N.: Mid to late Holocene climate variability,  
923 forest fires and floods entwined with human occupation in the upper Ganga catchment, India,  
924 *Quaternary Science Reviews*, 293, 107725, <https://doi.org/10.1016/j.quascirev.2022.107725>,  
925 2022.

926 Sinha, R., Mohanta, H., Jain, V., and Tandon, S. K.: Geomorphic diversity as a river  
927 management tool and its application to the Ganga River, India, *River Research & Apps*, 33,  
928 1156–1176, <https://doi.org/10.1002/rra.3154>, 2017.

929 Snyder, N. P., Whipple, K. X., Tucker, G. E., and Merritts, D. J.: Importance of a stochastic



930 distribution of floods and erosion thresholds in the bedrock river incision problem, *J. Geophys.*  
931 *Res.*, 108, 2001JB001655, <https://doi.org/10.1029/2001JB001655>, 2003.

932 Srivastava, P., Kumar, A., Chaudhary, S., Meena, N., Sundriyal, Y. P., Rawat, S., Rana, N.,  
933 Perumal, R. J., Bisht, P., Sharma, D., Agnihotri, R., Bagri, D. S., Juyal, N., Wasson, R. J., and  
934 Ziegler, A. D.: Paleofloods records in Himalaya, *Geomorphology*, 284, 17–30,  
935 <https://doi.org/10.1016/j.geomorph.2016.12.011>, 2017.

936 Starke, J., Ehlers, T. A., and Schaller, M.: Latitudinal effect of vegetation on erosion rates  
937 identified along western South America, *Science*, 367, 1358–1361,  
938 <https://doi.org/10.1126/science.aaz0840>, 2020.

939 Tibau, X.-A., Reimers, C., Gerhardus, A., Denzler, J., Eyring, V., and Runge, J.: A  
940 spatiotemporal stochastic climate model for benchmarking causal discovery methods for  
941 teleconnections, *Environ. Data Science*, 1, e12, <https://doi.org/10.1017/eds.2022.11>, 2022.

942 Ullah, W., Wang, G., Lou, D., Ullah, S., Bhatti, A. S., Ullah, S., Karim, A., Hagan, D. F. T., and  
943 Ali, G.: Large-scale atmospheric circulation patterns associated with extreme monsoon  
944 precipitation in Pakistan during 1981–2018, *Atmospheric Research*, 253, 105489,  
945 <https://doi.org/10.1016/j.atmosres.2021.105489>, 2021.

946 Vellore, R. K., Kaplan, M. L., Krishnan, R., Lewis, J. M., Sabade, S., Deshpande, N., Singh, B.  
947 B., Madhura, R. K., and Rama Rao, M. V. S.: Monsoon-extratropical circulation interactions in  
948 Himalayan extreme rainfall, *Clim Dyn*, 46, 3517–3546, [https://doi.org/10.1007/s00382-015-](https://doi.org/10.1007/s00382-015-2784-x)  
949 [2784-x](https://doi.org/10.1007/s00382-015-2784-x), 2016.

950 Wang, N., Zeng, X.-M., Guo, W.-D., Chen, C., You, W., Zheng, Y., and Zhu, J.: Quantitative  
951 diagnosis of moisture sources and transport pathways for summer precipitation over the mid-  
952 lower Yangtze River Basin, *Journal of Hydrology*, 559, 252–265,  
953 <https://doi.org/10.1016/j.jhydrol.2018.02.003>, 2018.

954 Whipple, K. X. and Tucker, G. E.: Dynamics of the stream-power river incision model:  
955 Implications for height limits of mountain ranges, landscape response timescales, and research  
956 needs, *J. Geophys. Res.*, 104, 17661–17674, <https://doi.org/10.1029/1999JB900120>, 1999.

957 Whipple, K. X., Hancock, G. S., and Anderson, R. S.: River incision into bedrock: Mechanics  
958 and relative efficacy of plucking, abrasion, and cavitation, *Geological Society of America*  
959 *Bulletin*, 112, 490–503, [https://doi.org/10.1130/0016-7606\(2000\)112<490:RIIBMA>2.0.CO;2](https://doi.org/10.1130/0016-7606(2000)112<490:RIIBMA>2.0.CO;2),  
960 2000.

961 Wobus, C., Whipple, K. X., Kirby, E., Snyder, N., Johnson, J., Spyropolou, K., Crosby, B., and  
962 Sheehan, D.: Tectonics from topography: Procedures, promise, and pitfalls, in: *Tectonics,*  
963 *Climate, and Landscape Evolution*, Geological Society of America,  
964 [https://doi.org/10.1130/2006.2398\(04\)](https://doi.org/10.1130/2006.2398(04)), 2006.

965 Wolfensberger, D., Gabella, M., Boscacci, M., Germann, U., and Berne, A.: RainForest: a  
966 random forest algorithm for quantitative precipitation estimation over Switzerland, *Atmos. Meas.*  
967 *Tech.*, 14, 3169–3193, <https://doi.org/10.5194/amt-14-3169-2021>, 2021.

968 Wu, K., Liu, S., Jiang, Z., Liu, Q., Zhu, Y., Yi, Y., Xie, F., Ahmad Tahir, A., and Saifullah, M.:  
969 Quantification of glacier mass budgets in the Karakoram region of Upper Indus Basin during the  
970 early twenty-first century, *Journal of Hydrology*, 603, 127095,  
971 <https://doi.org/10.1016/j.jhydrol.2021.127095>, 2021.

972 Zeitler, P. K., Koons, P. O., Bishop, M. P., Chamberlain, C. P., Craw, D., Edwards, M. A.,  
973 Hamidullah, S., Jan, M. Q., Khan, M. A., Khattak, M. U. K., Kidd, W. S. F., Mackie, R. L.,  
974 Meltzer, A. S., Park, S. K., Pecher, A., Poage, M. A., Sarker, G., Schneider, D. A., Seeber, L.,  
975 and Shroder, J. F.: Crustal reworking at Nanga Parbat, Pakistan: Metamorphic consequences of  
976 thermal-mechanical coupling facilitated by erosion, *Tectonics*, 20, 712–728,  
977 <https://doi.org/10.1029/2000TC001243>, 2001.

978 Zeitler, P.K., Meltzer, A.S., Brown, L., Kidd, W.S., Lim, C., Enkelmann, E., 2014. Tectonics and  
979 topographic evolution of Namche Barwa and the easternmost Lhasa block, Tibet, in: *Toward an*  
980 *Improved Understanding of Uplift Mechanisms and the Elevation History of the Tibetan Plateau.*  
981 *Geological Society of America Special Papers*, pp. 23–58.  
982